

Supplement to: State of Wildfires 2023-24

Matthew W. Jones, Douglas I. Kelley, Chantelle A. Burton, Francesca Di Giuseppe, et al.

To accompanying the pre-print available at:
Earth System Science Data Discussions

Supplementary Figures

Figures referred to in the main text.

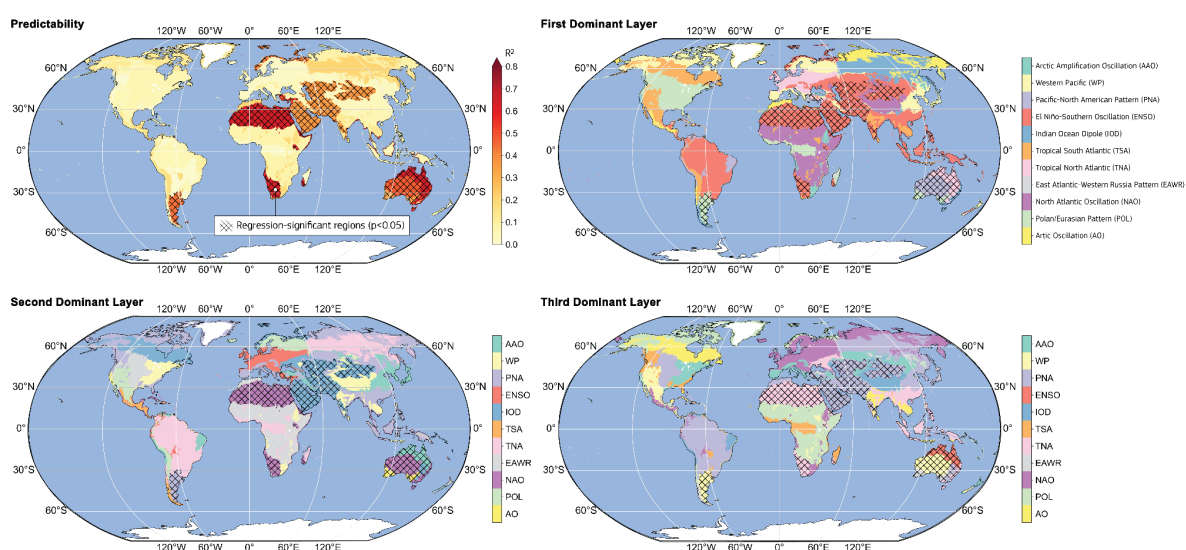
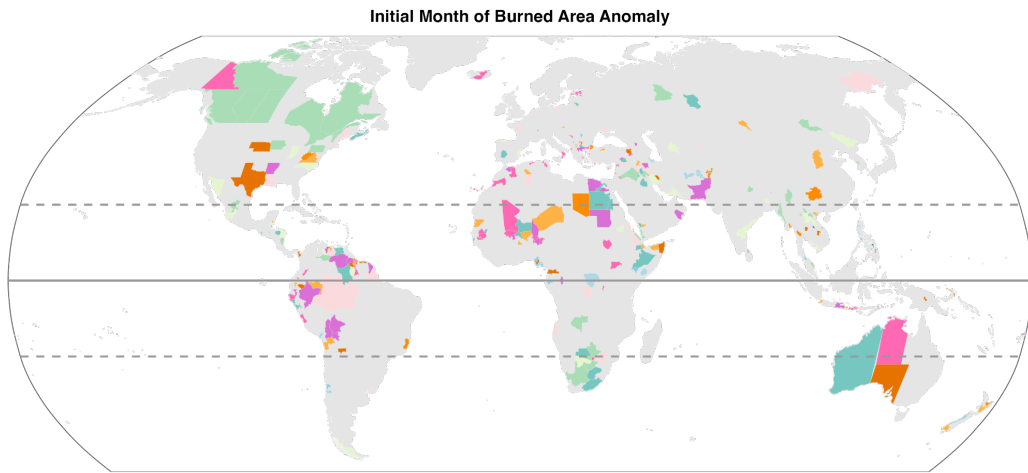
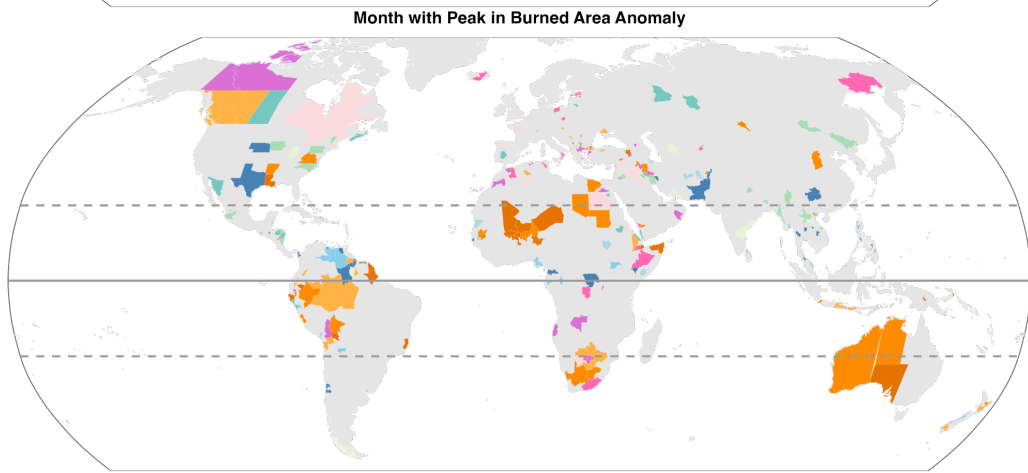


Figure S1: Influence of modes of climate variability on Burned Area (BA) in the period 2001-2020. The figure maps the mode of climate variability with a dominant (and secondary, and tertiary) influence on interannual variability in BA. The coefficient of covariation (R^2) value linking BA to each mode is also shown. The modes included are: Antarctic Oscillation (AAO); West Pacific (WP) pattern; Pacific–North American (PNA) pattern; El Niño–Southern Oscillation (ENSO); Indian Ocean Dipole (IOD); tropical South Atlantic (TSA) pattern; tropical North Atlantic (TNA) pattern; East Atlantic/Western Russia (EAWR) pattern; North Atlantic Oscillation (NAO); Polar-Eurasian (POL) pattern; and the Arctic Oscillation (AO).

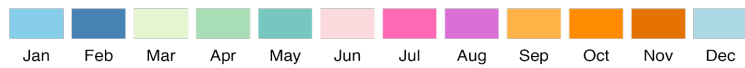
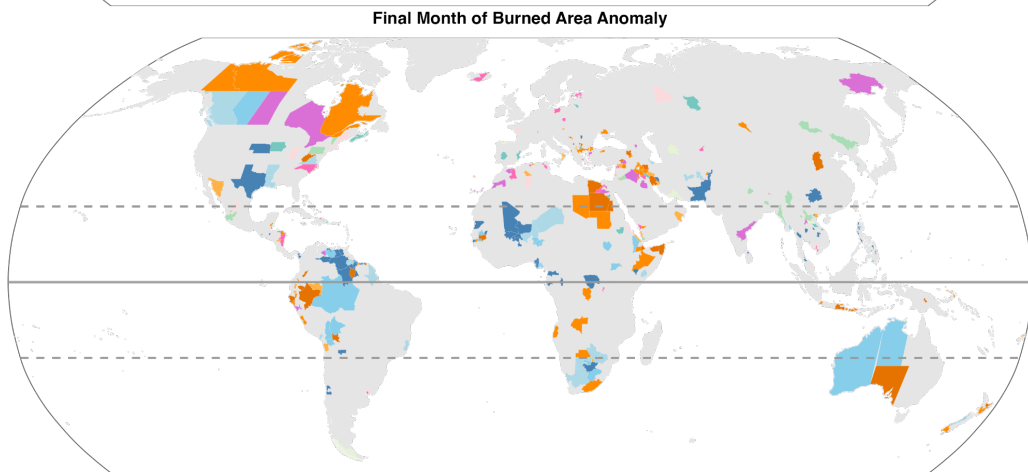
24



25

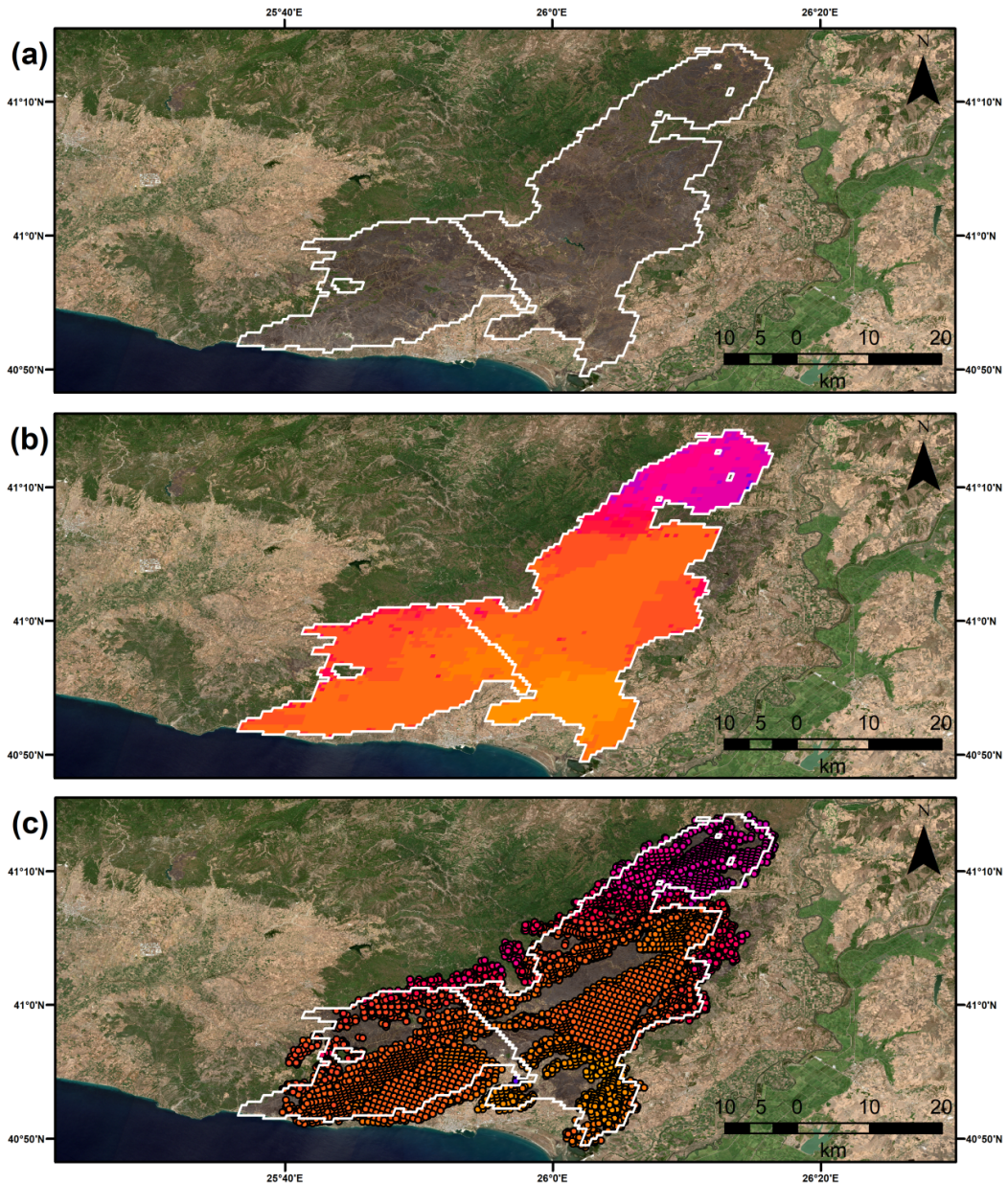


26
27



28
29
30
31
32
33
34

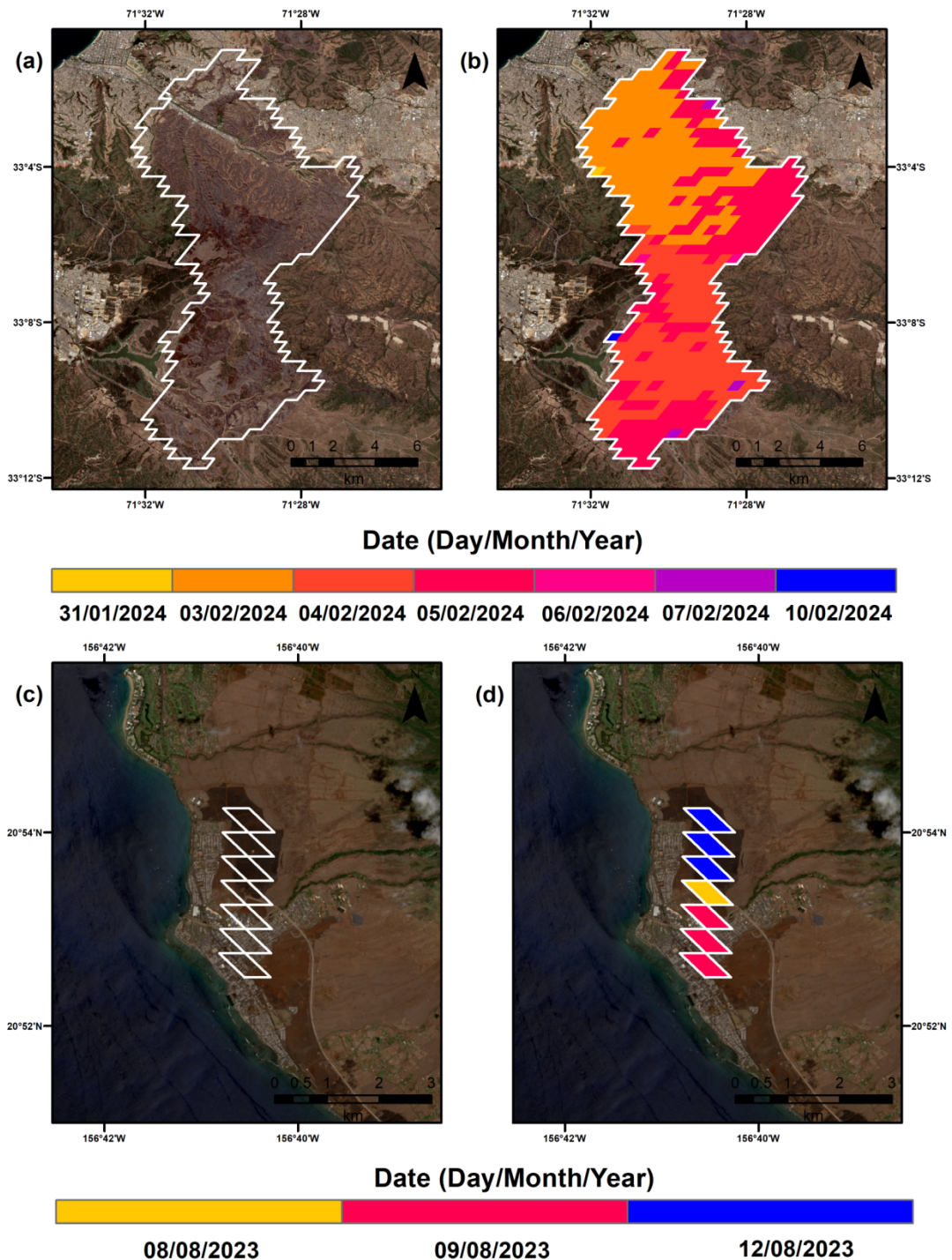
Figure S2: (Top panel) first month, **(middle panel)** peak month, and **(lower panel)** final month of positive BA anomalies at Global Administrative Level 1 during March 2023-February 2024. Peak anomalies are identified relative to the monthly climatology in 2001-2023. The first and final months of the BA anomaly incorporate the period when BA was continuously above the climatological mean. Graduated colours are separated seasonally.



14/08 17/08 19/08 20/08 21/08 22/08 23/08 24/08 25/08 26/08 27/08 28/08 29/08 30/08 31/08 01/09 02/09 03/09 06/09 10/09 11/09

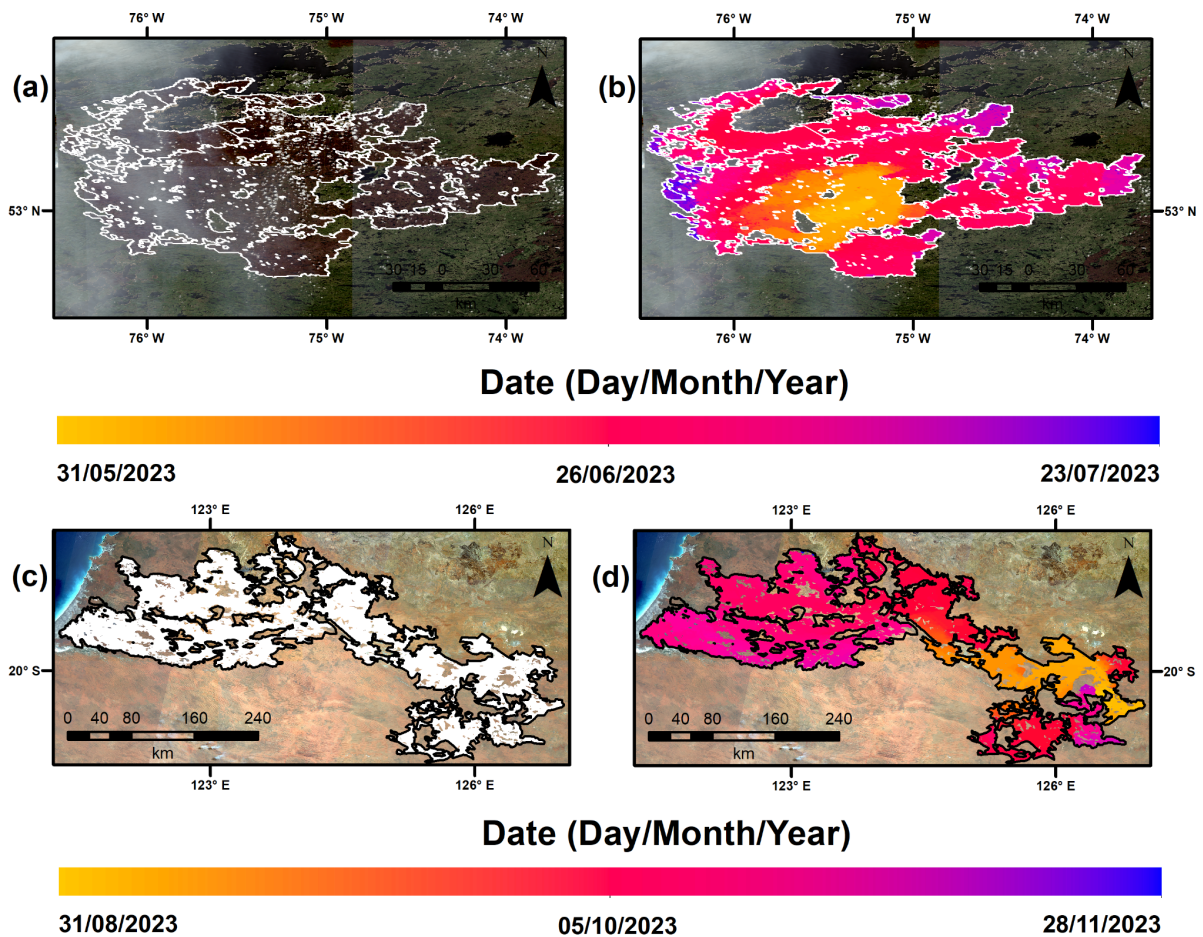
35
36
37
38
39
40
41
42
43
44
45
46

Figure S3: Perimeter and daily progression of the largest fire ever recorded in the EU (Xanthopoulos et al., 2024; EU Science Hub, 2023), near Alexandroupolis in Macedonia and Thrace, Greece. Panel (a) shows a Sentinel-2 true colour composite image (10 m resolution) from 12th September 2023, the day after the fire ceased to grow. The darker colour of recently-burned surfaces contrasts with green unburned forests in surrounding areas. Overlaying the image are lines marking the perimeter of the Alexandroupolis fire from the Global Fire Atlas. Panel (b) additionally shows the burn date according to the MODIS BA dataset MCD64A1 (500 m resolution), and for comparison panel (c) shows the burn date from active fire detections from the Visible Infrared Imaging Radiometer Suite (VIIRS) sensor (375 m resolution; Schroeder et al., 2014).

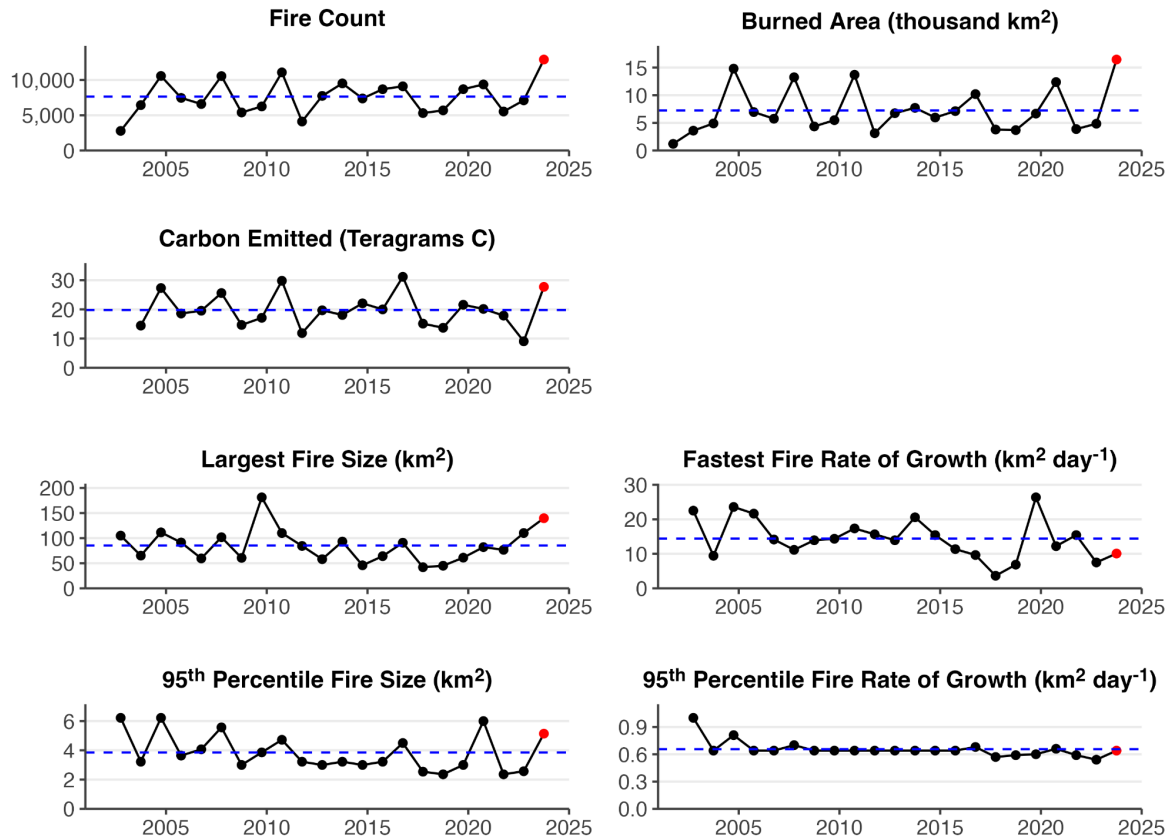


47
48
49
50
51
52
53
54

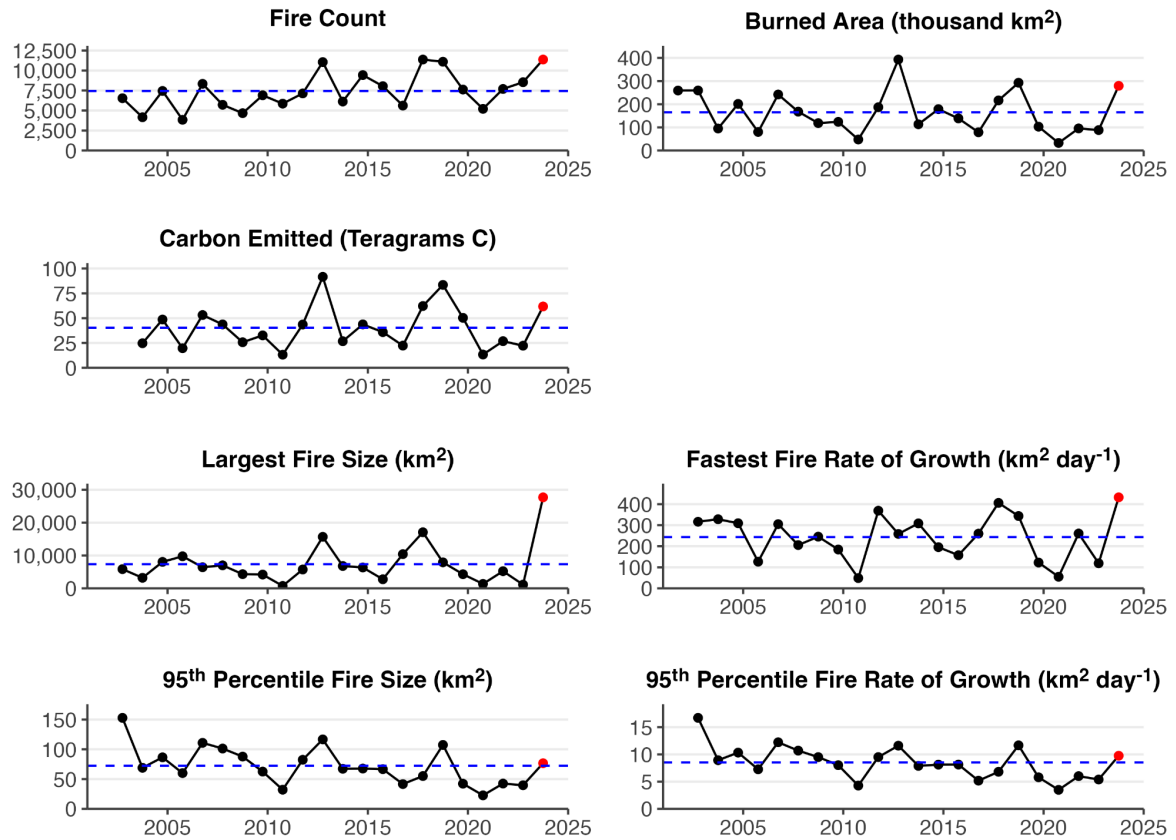
Figure S4: Perimeter and daily progression of extreme individual fires in (a-b) Valparaíso, Chile, and (c-d) Lahaina, Hawai'i. Panels (a) and (c) show Sentinel-2 true colour composite images (10 m resolution) from 8th March 2024 and 18th August 2023, on the first cloud-free day after each fire. Overlaying the image are lines marking the perimeter of the impactful fire events from the Global Fire Atlas. Panels (b) and (d) additionally show the burn date according to the MODIS BA dataset MCD64A1 (500 m resolution).



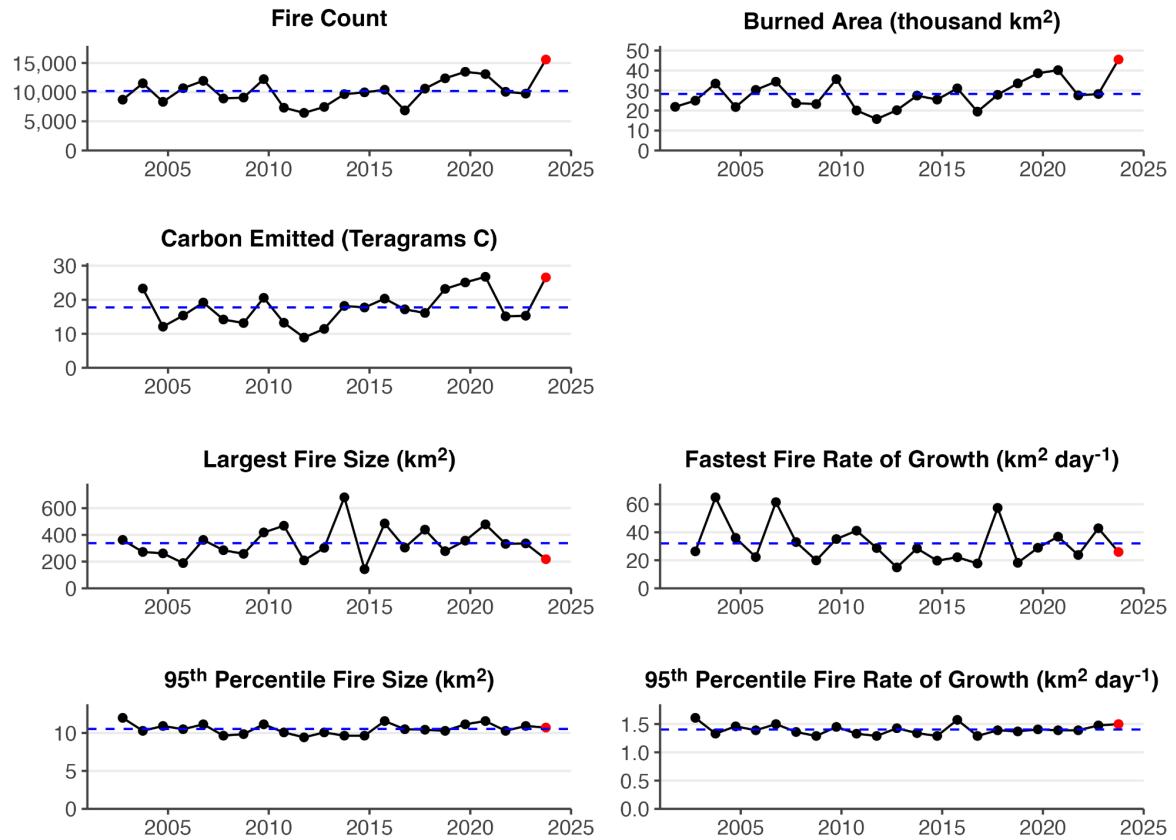
55
 56 **Figure S5:** Perimeter and daily progression of extreme individual fires (a-b) near La Grande
 57 Reservoir in Quebec, Canada, and (c-d) in the Great Sandy Desert and Anna Plains,
 58 Australia. Panels (a) and (c) show Sentinel-2 true colour composite images (10 m resolution)
 59 based on observations in the periods 25/04/2023-25/08/2023 and 02/09/2023 to 08/09/2023,
 60 respectively. Overlaying the image (a) are white lines marking the perimeter of the La Grande
 61 fire according to the Global Fire Atlas. Overlaying the image (c) are white areas marking the
 62 area burned by the La Grande fire according to the Global Fire Atlas, and black lines marking
 63 the wildfire perimeter from the Department of Fire and Emergency Services in Western
 64 Australia. Panels (b) and (d) additionally show the burn date according to the MODIS BA
 65 dataset MCD64A1 (500 m resolution).
 66



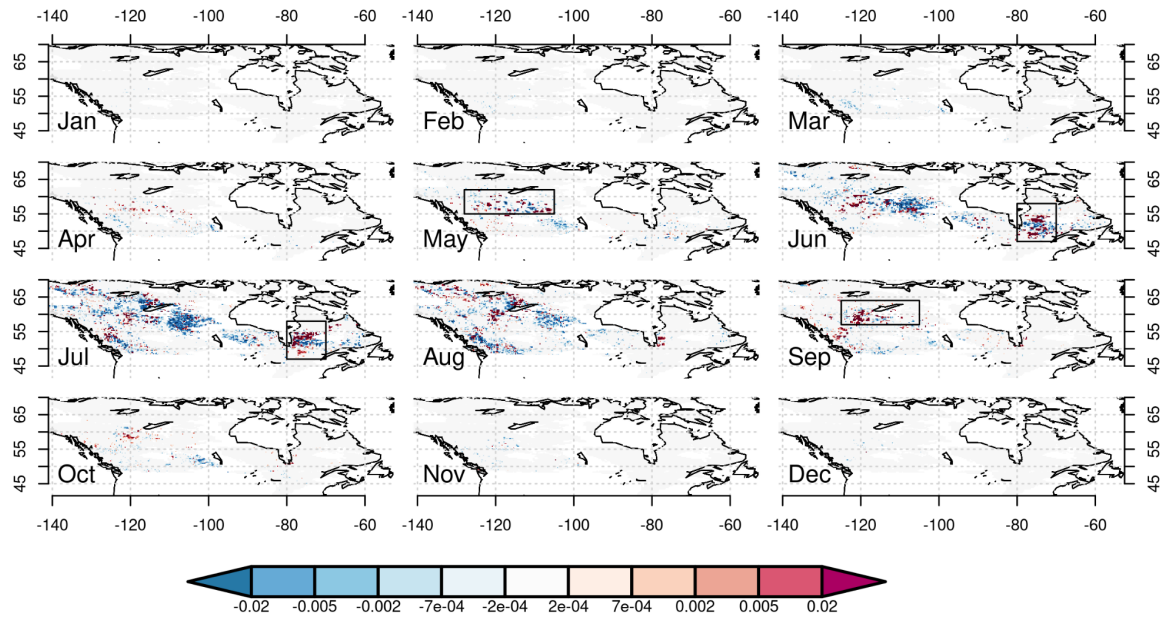
67
 68 **Figure S6:** Summary of the 2023-2024 fire season in Lao PDR. Time series of annual fire
 69 count, BA, C emissions, PM2.5 emissions, 95th percentile fire size, fastest daily rate of growth,
 70 and 95th percentile fire daily rate of growth. Black dots show annual values prior to the latest
 71 fire season, red dots the values during the latest fire season, and blue dashed lines the
 72 average values across all fire seasons.



73
 74 **Figure S7:** Summary of the 2023-2024 fire season in the state of Western Australia. Time
 75 series of annual fire count, BA, C emissions, PM2.5 emissions, 95th percentile fire size, fastest
 76 daily rate of growth, and 95th percentile fire daily rate of growth. Black dots show annual values
 77 prior to the latest fire season, red dots the values during the latest fire season, and blue dashed
 78 lines the average values across all fire seasons.

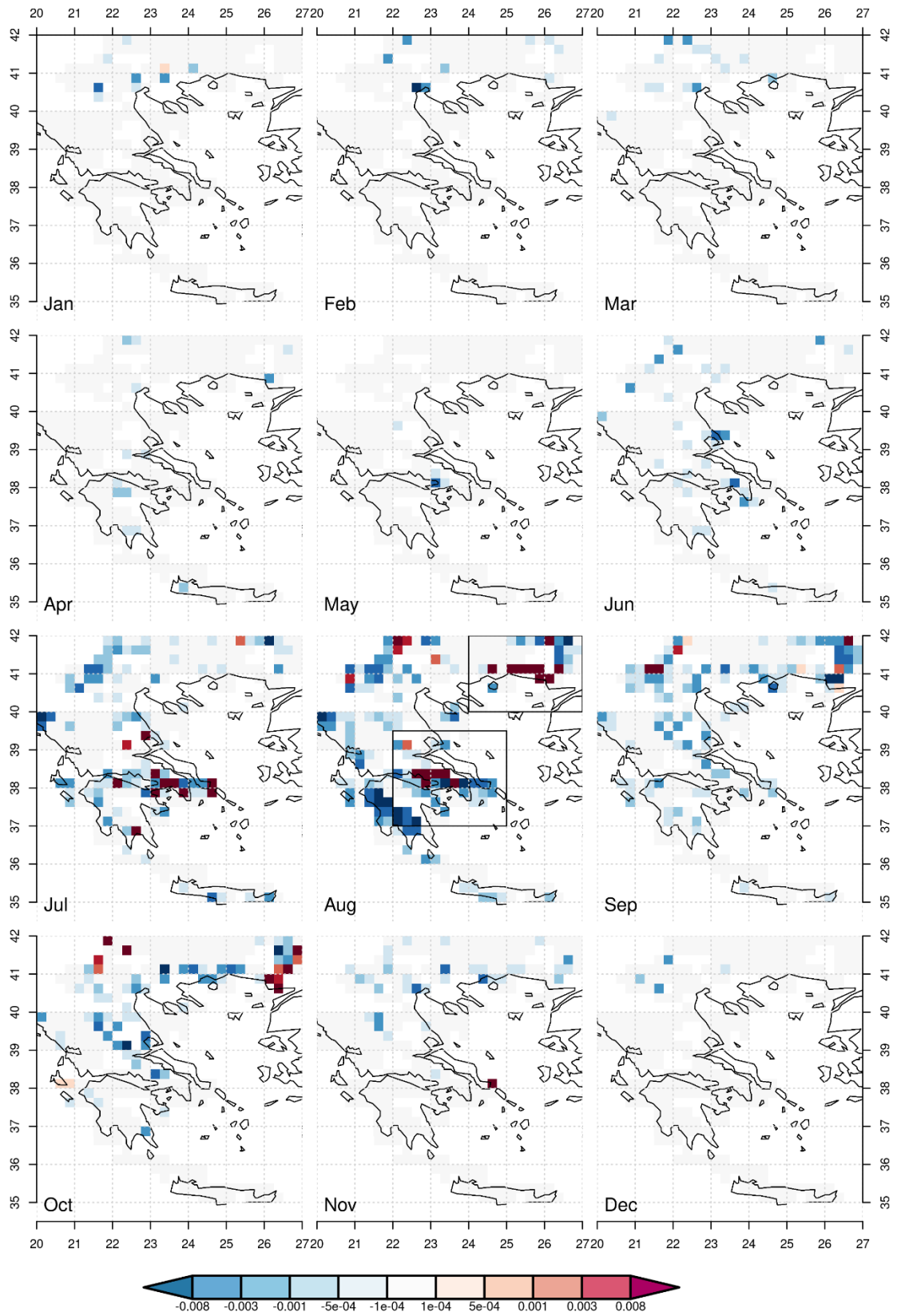


79
80 **Figure S8:** Summary of the 2023-2024 fire season in Venezuela. Time series of annual fire
81 count, BA, C emissions, PM2.5 emissions, 95th percentile fire size, fastest daily rate of growth,
82 and 95th percentile fire daily rate of growth. Black dots show annual values prior to the latest
83 fire season, red dots the values during the latest fire season, and blue dashed lines the
84 average values across all fire seasons.
85

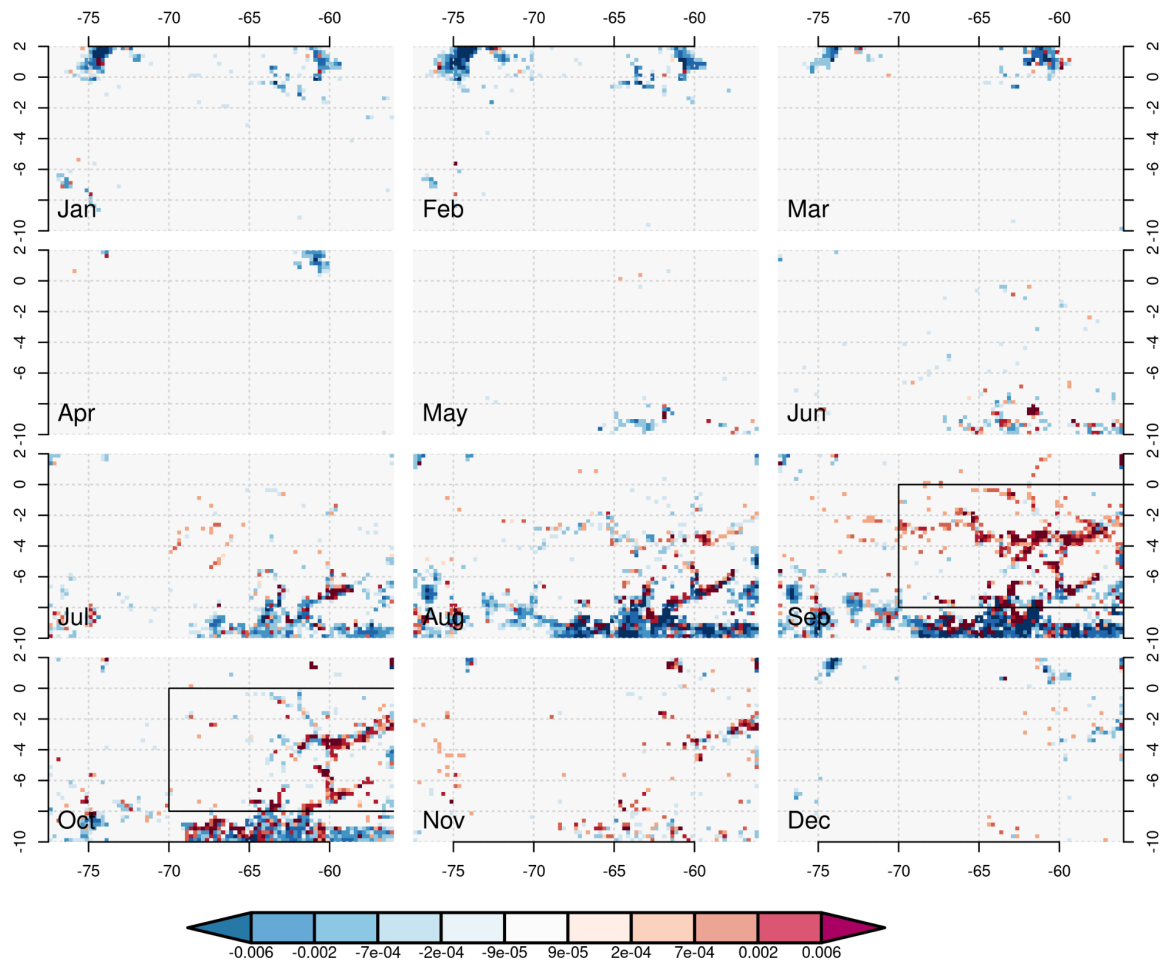


86
87
88
89
90

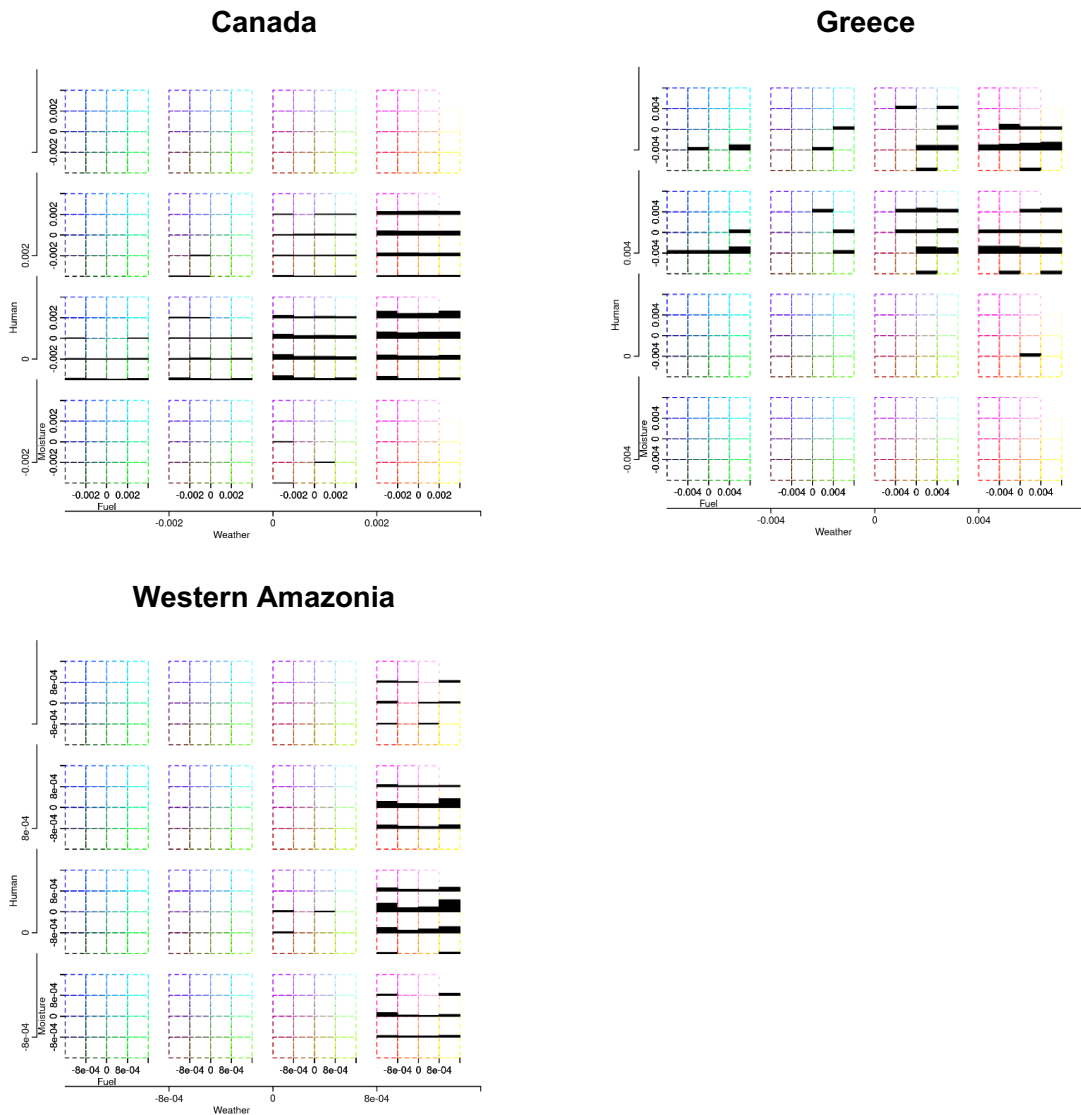
Figure S9: Monthly BA fraction anomaly at 0.25° for Canada for 2023 compare 2001-2023 climatological average. Boxes indicate focal months and regions in driver attribution (Section 3.3.7).



91
92 **Figure S10:** Same as **Figure S9** for Greece

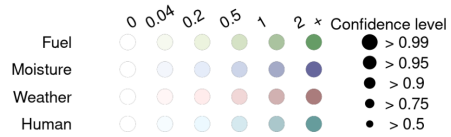
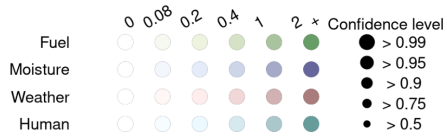
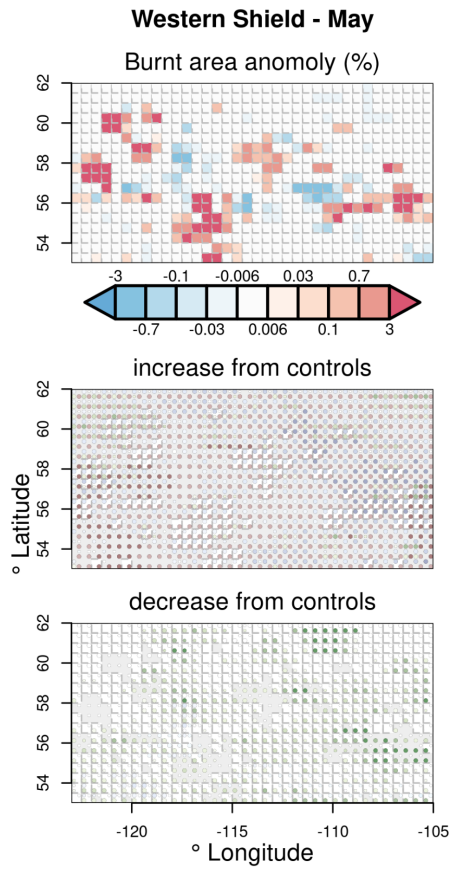
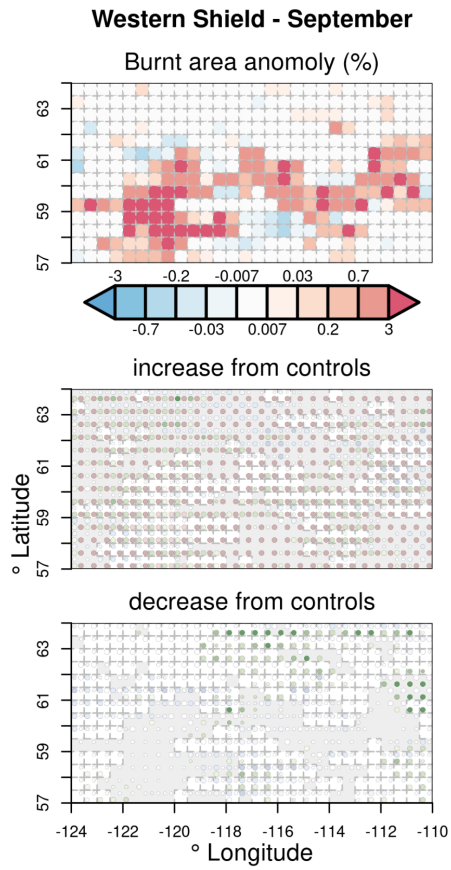


93
 94 **Figure S11:** Same as **Figure S9** for Western Amazonia
 95
 96
 97



100
101
102
103
104
105
106
107
108
109
110
111

Figure S12: shows the co-occurrence of anomalies for 2023 of our four controls in different regions. In each box of 16 bins, the bottom left corresponds to the negative influence of fuel and moisture on fire anomalies, the top is the positive influence of fuel moisture, and the right indicates a positive influence of fuel load. The bottom left box indicates the negative influence of fire weather and humans, while the right boxes indicate the positive influence of fire weather, and the top indicates the positive influence of humans. The shading of each bin for each region indicates how much of that region falls into that bin. The shades themselves represent the uncertainty range, with grey indicating the 10th percentile and black indicating the 90th percentile.

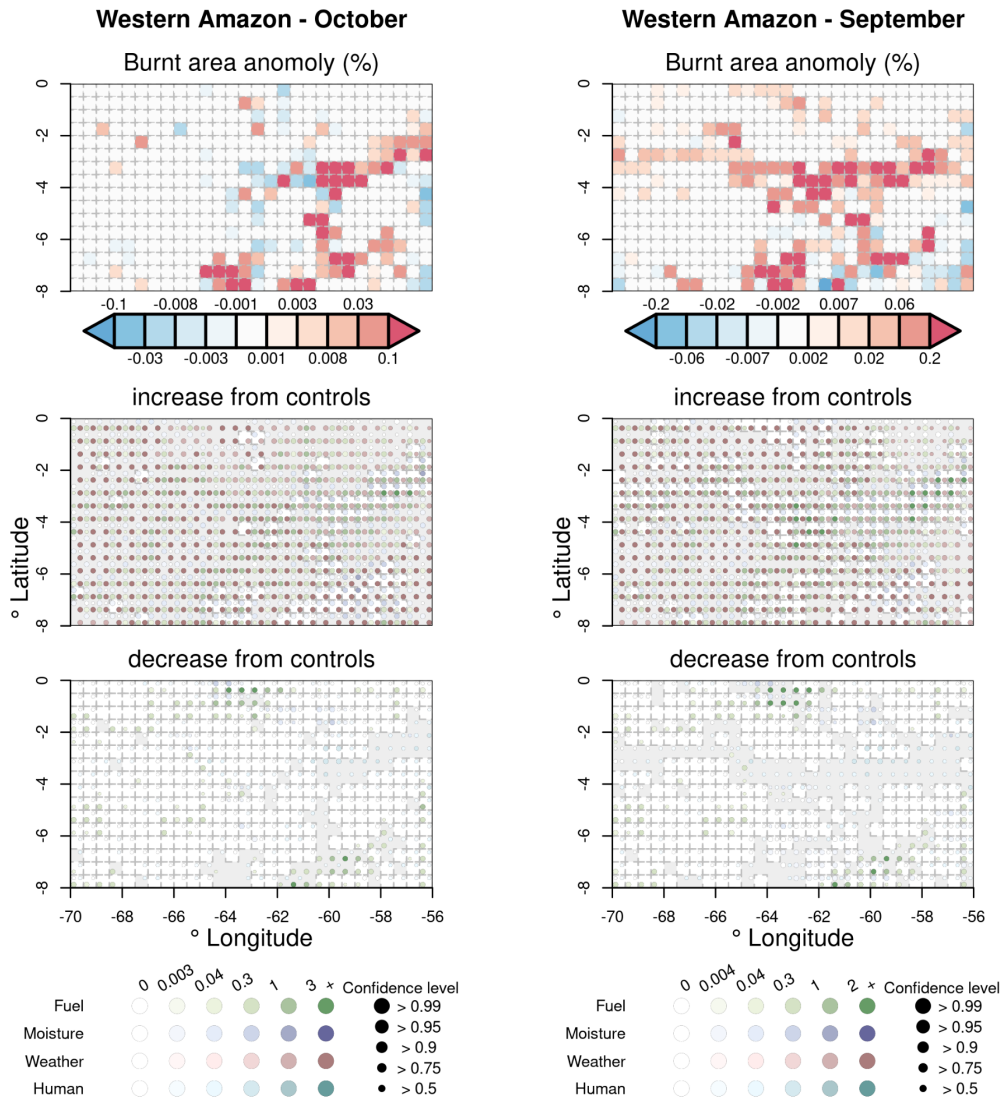


112

113 **Figure S13:** Same as **Figure 15** but for the Canadian Western Shield.

114

115



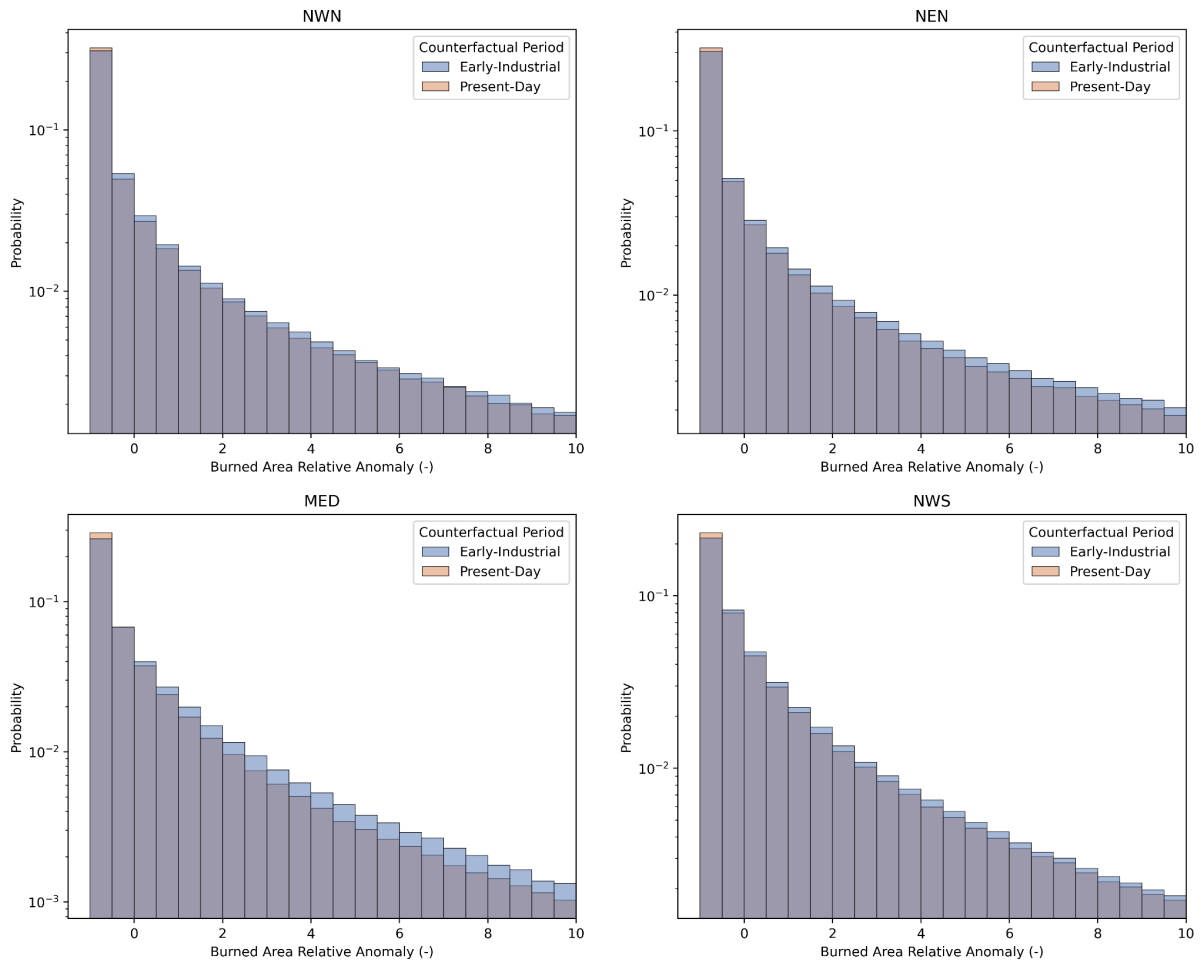
116

117 **Figure S14:** Same as **Figure 15** but for Western Amazonia.

118

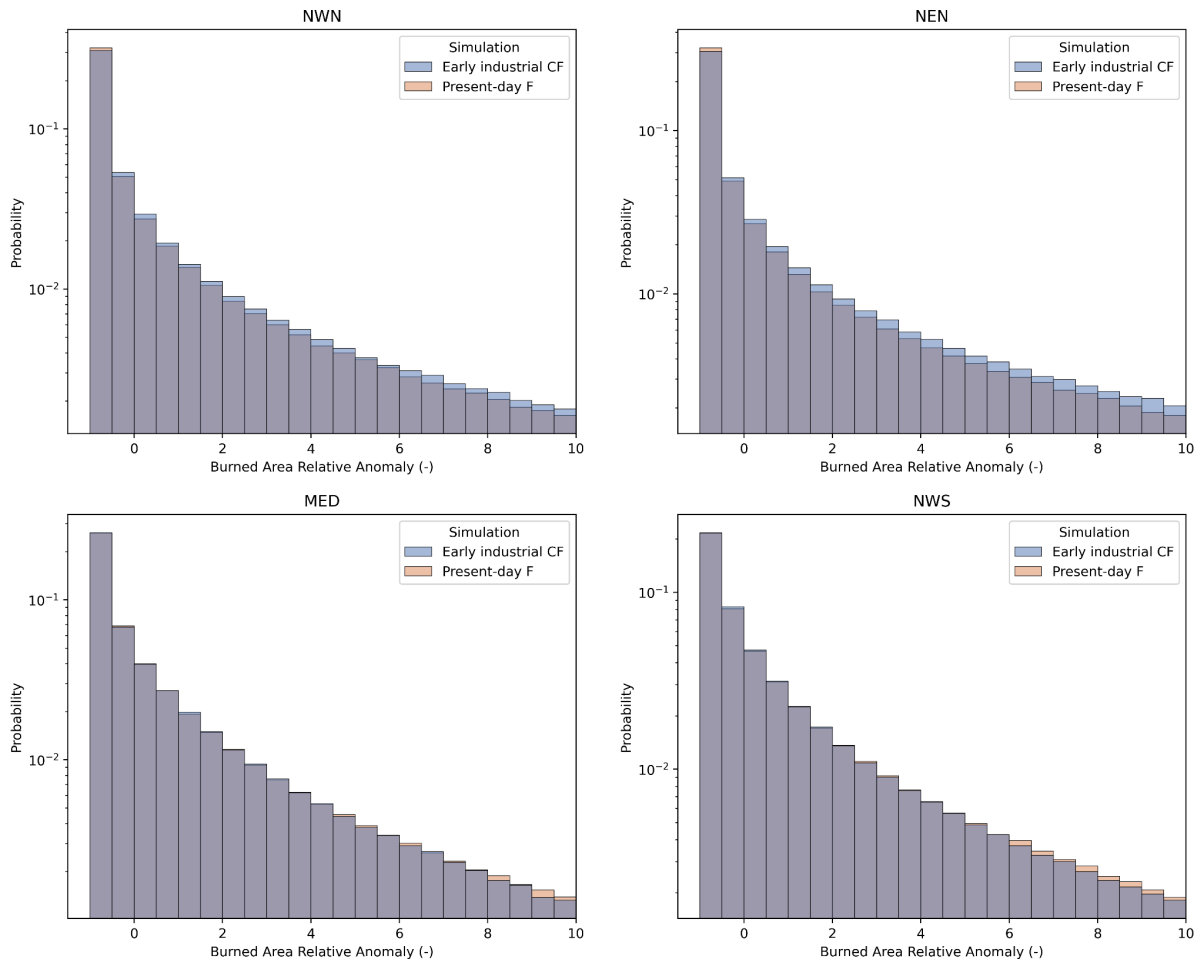
119

120



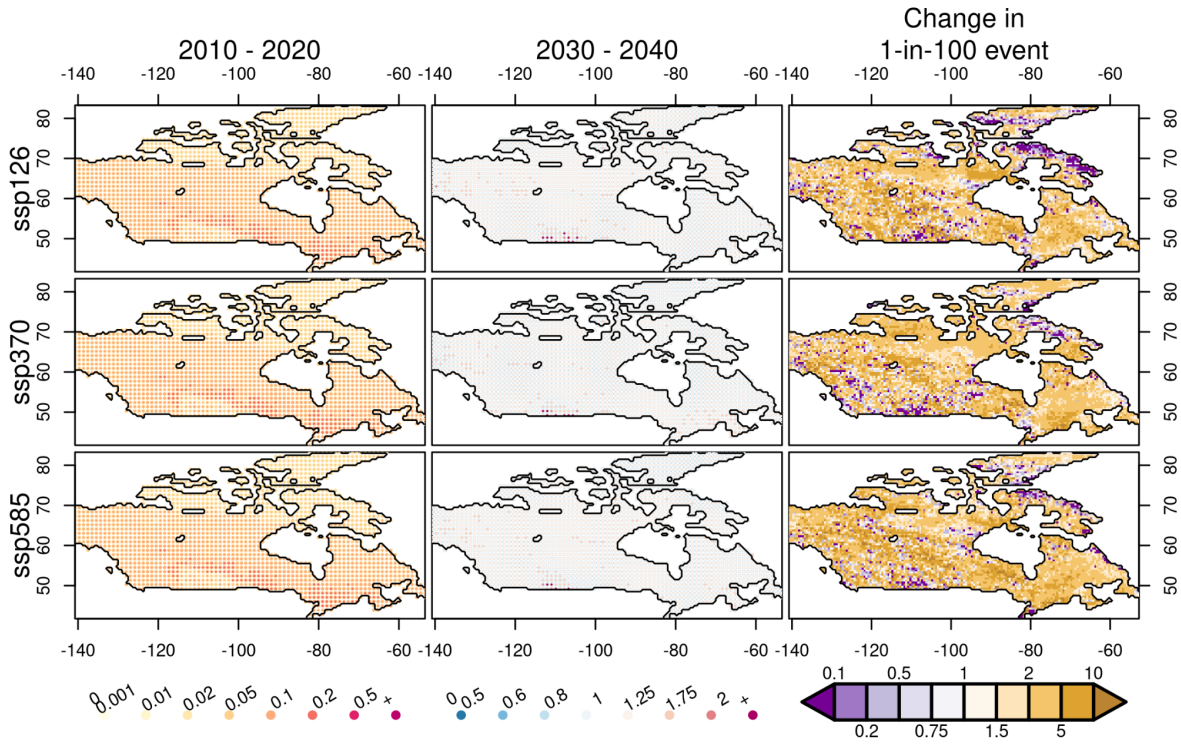
121
 122
 123
 124
 125
 126
 127
 128

Figure S15: Change in median BA anomaly due to socioeconomic factors (population and land-use change) from FireMIP. Present day BA (2003-2019) for counterfactual (detrended climate, orange) compared to early-industrial (1901-1917) in the counterfactual (detrended climate, blue), for AR6 regions. Top row: North West North America (NWN, LEFT) and North East North America NEN (RIGHT). Bottom row: Mediterranean (MED, LEFT), and North West South America (NWS, RIGHT). Probability is shown on a log scale.



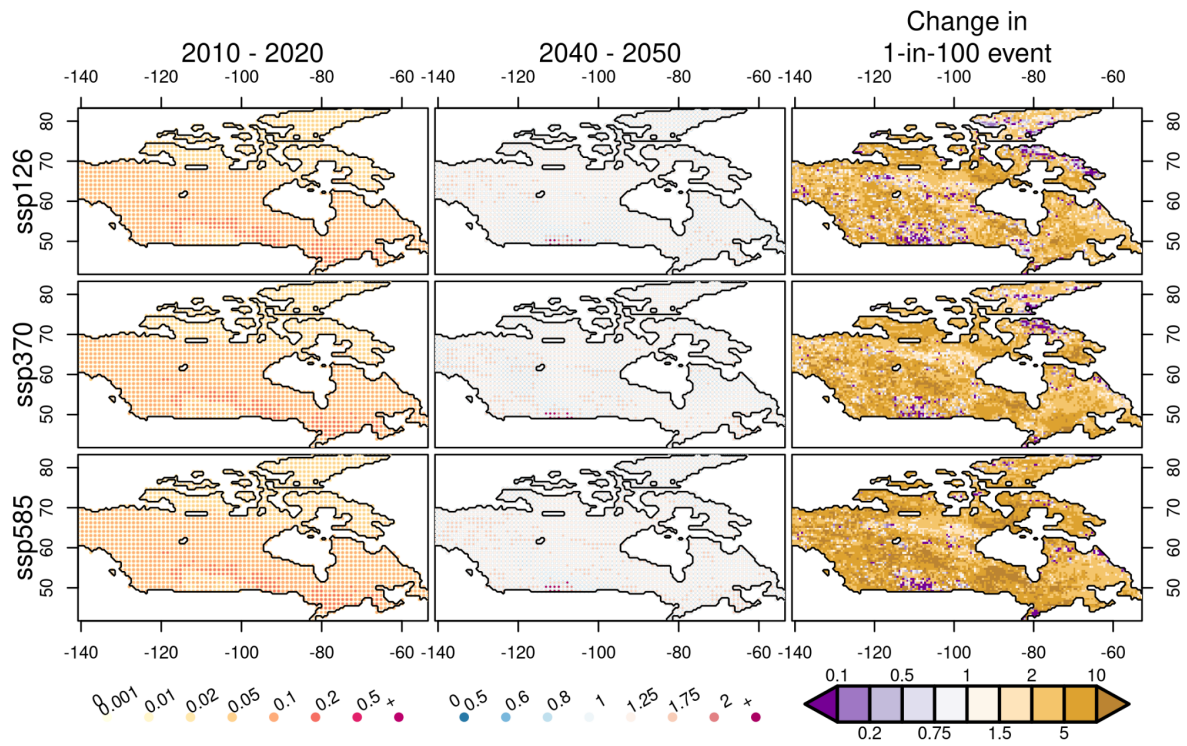
129
 130 **Figure S16:** Change in median BA anomaly due to all forcing (climate change and
 131 socioeconomic factors) from FireMIP. Present day BA (2003-2019) for factual (historical
 132 forcing, orange) compared to early-industrial (1901-1917) in the counterfactual (detrended
 133 climate, blue), for AR6 regions. Top row: North West North America (NWN, LEFT) and North
 134 East North America NEN (RIGHT). Bottom row: Mediterranean (MED, LEFT), and North West
 135 South America (NWS, RIGHT). Probability is shown on a log scale.
 136

137
138
139
140
141
142
143
144



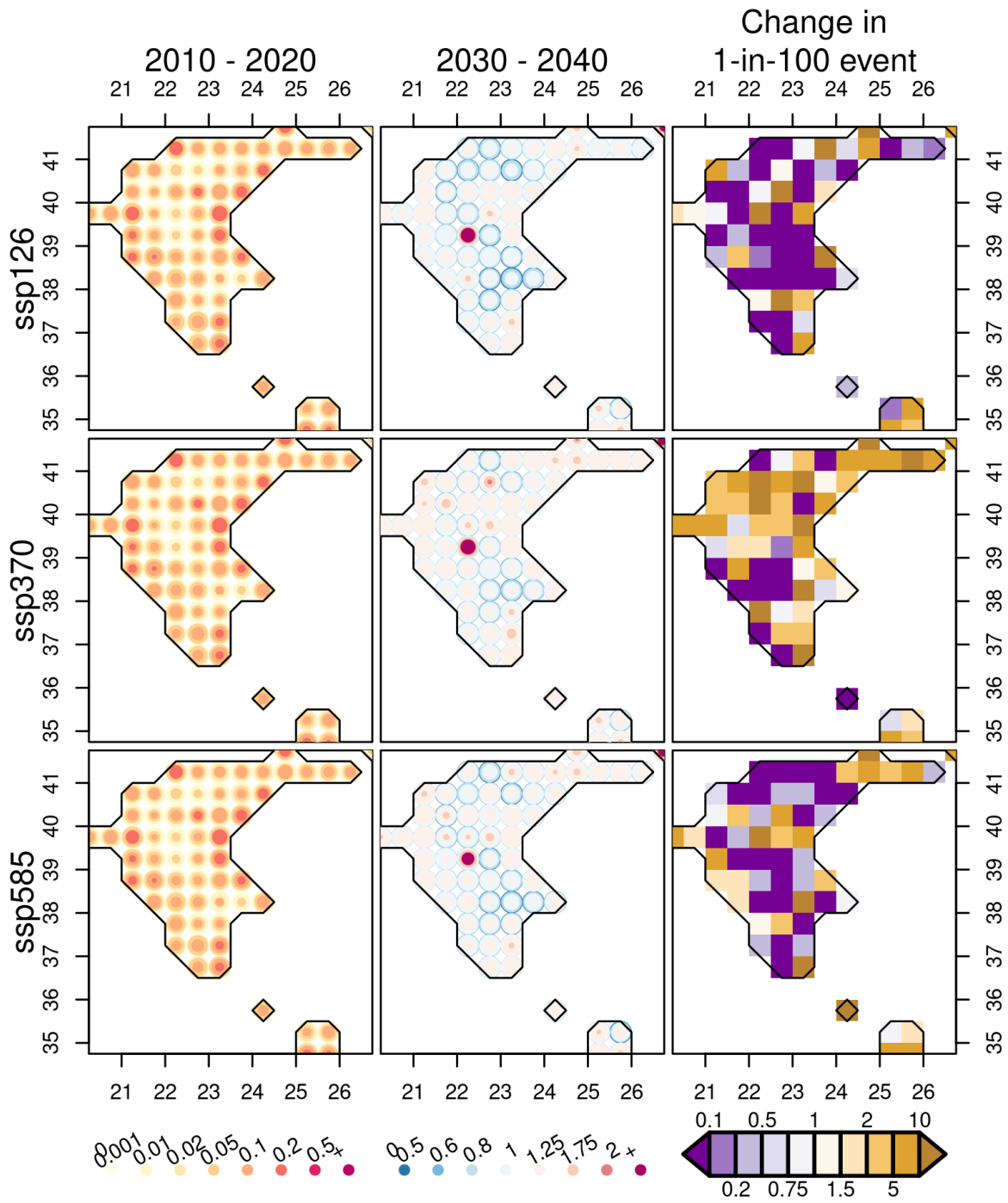
145
146

Figure S17: Same as Figure 23 but covering 2030-2040



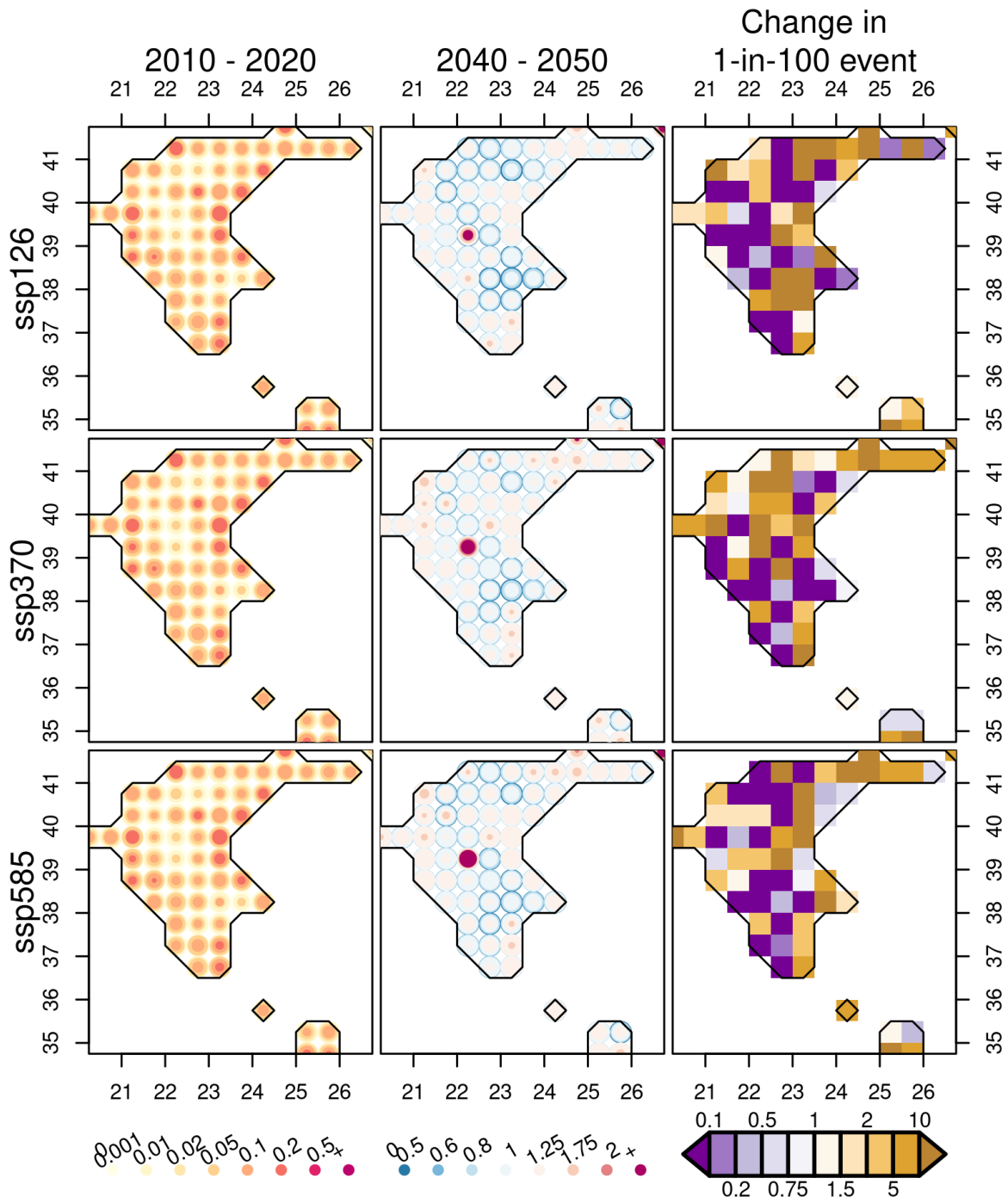
147
148

Figure S18: Same as **Figure 23** but covering 2040-2050



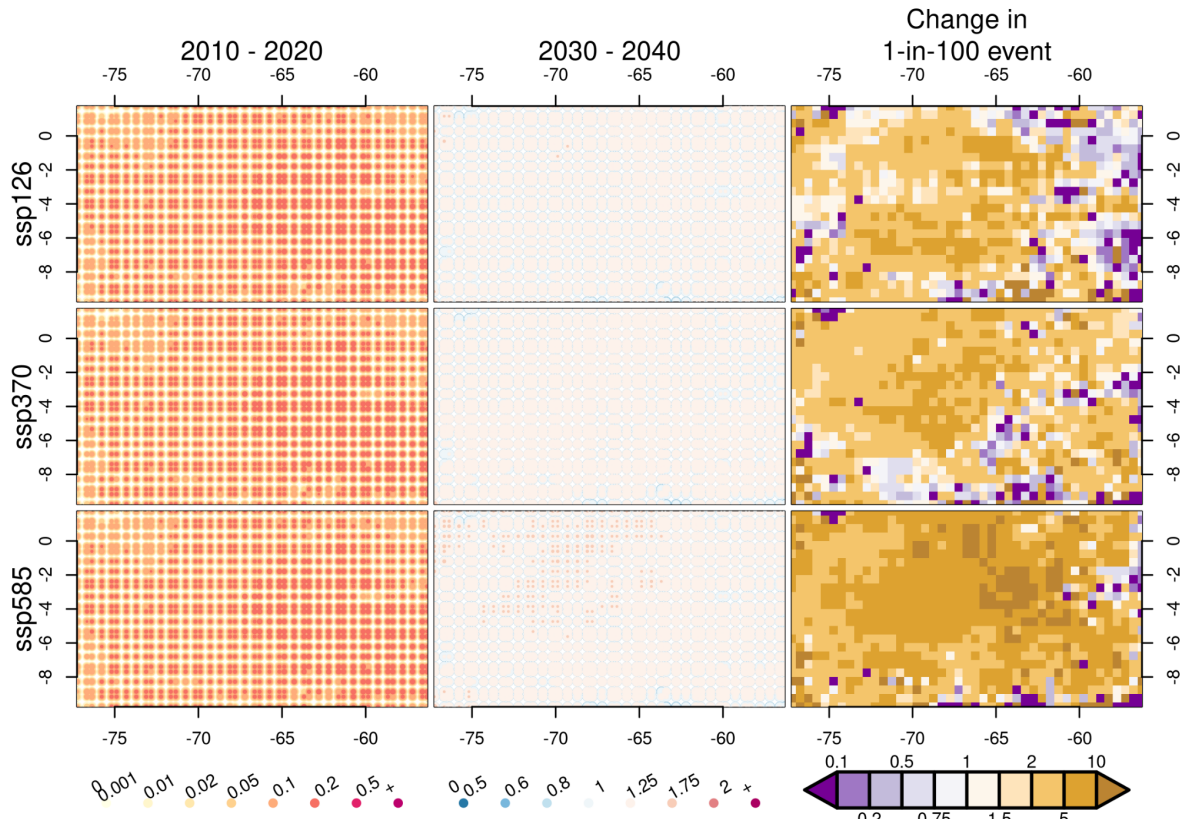
149
150

Figure S19: Same as **Figure 24** but covering 2030-2040



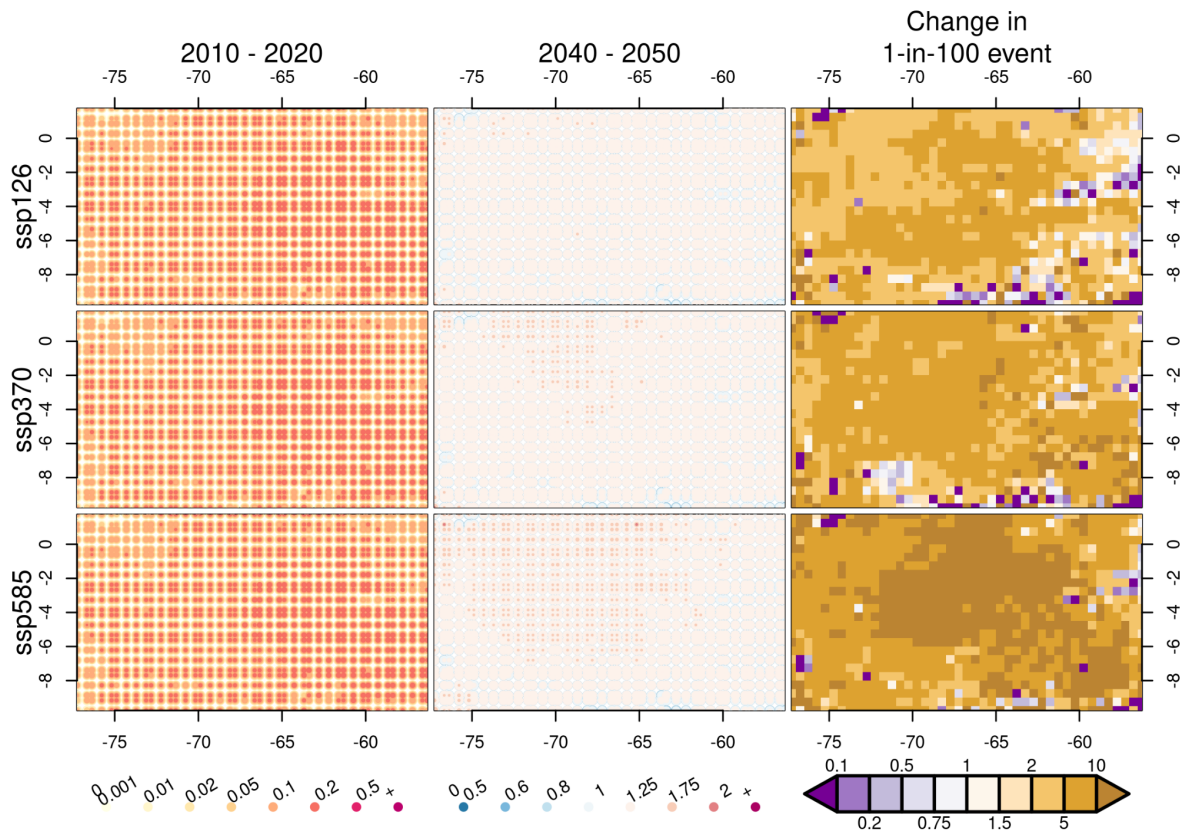
151
152
153
154

Figure S20: Same as **Figure 24** but covering 2040-2050



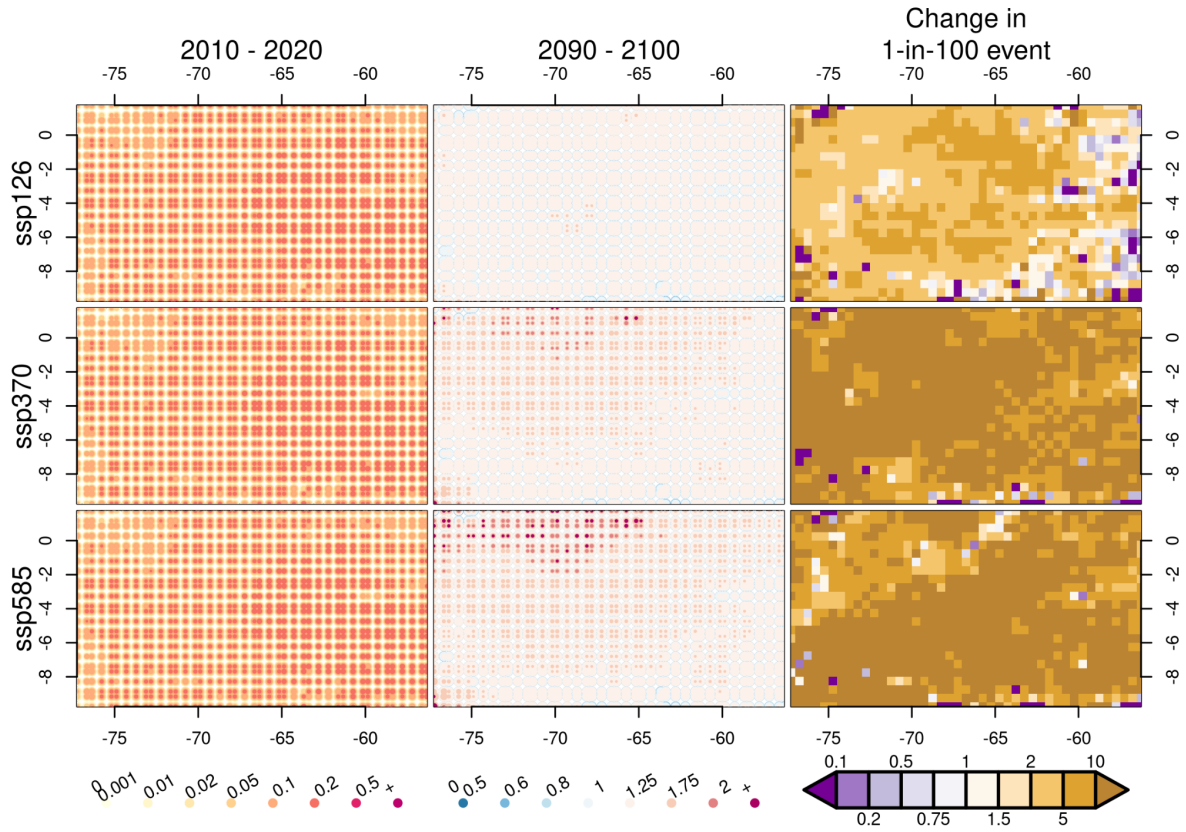
156
157
158
159

Figure S21: Same as **Figure 23** but Western Amazonia covering 2030-2040 August-October.



160
161

Figure S22: Same as **Figure S21** but covering 2040-2050



163
164
165
166
167

Figure 23: Same as Figure S21 but for 2090-2100.

168 Extended Methods

169

170 *Data and Data Processing*

171

172 *ConFire vegetation fraction driving data*

173

174 In **Section 2.4.4.1**, we drive ConFire with tree and non-tree vegetated cover from the Joint
175 UK Land Environment Simulator Earth System impacts model (JULES-ES) at version 5.5
176 (Clark et al., 2011; Mathison et al., 2023)) driven with GSWP3-W5E5 forcings provided at a
177 0.5° spatial resolution by ISIMIP3a. These runs are freely available at
178 <https://www.isimip.org/impactmodels/details/292/>. JULES-ES dynamically models vegetation
179 cover in response to meteorology, hydrology, nitrogen availability, and land use change.
180 JULES-ES has been extensively evaluated against snapshots and site-based measurements
181 of vegetation cover and carbon (Mathison et al., 2023; Burton et al., 2022; Clark et al., 2011;
182 Burton et al., 2019; Sellar et al., 2019). JULES-ES-ISIMIP has previously been used as driving
183 data for ConFire to perform future projections (UNEP et al., 2022), though using a previous
184 round of ISIMIP climate forcing (ISIMIP2b). As per (UNEP et al., 2022), vegetation responses
185 to JULES-ES’s internal fire model were turned off so as not to double-count the effects of
186 burning. However, in (UNEP et al., 2022), residual JULES-ES simulated biases in vegetation
187 cover were allowed to persist, increasing the uncertainty range of local vegetation cover and
188 resultant burned area responses. We therefore correct the bias in JULES-ES’s vegetation
189 cover using a trend-preserving empirical quantile mapping bias adjustment method,
190 implemented using the *ibicus* software package (Spuler et al., 2024). The method corrects the
191 bias induced by the JULES-ES model rather than the bias of the climate model, assuming that
192 this has been removed by the ISIMIP3BASD method (Lange, 2019).

193

194 The bias adjustment approach maps the empirical cumulative distribution function of each
195 surface cover type at each grid cell derived from the JULES-ES model output to the
196 corresponding quantiles in the MODIS VCF collection 6.1 remote sensed data (DiMiceli et al.,
197 2017) at this grid cell over the reference period (2002-2019). For Canada, where collection
198 6.1 does not extend north of 60DEG, we used collection 6 (Dimiceli and Others, 2015). This
199 mapping is subsequently applied to the surface information output from JULES-ES driven by
200 climate models over the historical (1994-2014) and future (2015-2099) period. To preserve
201 the trend in the vegetation cover over the future periods, additive detrending of the mean is
202 applied:

203

$$204 \quad x_{cm_fut} \rightarrow F_{obs}^{-1}(F_{cm_ref}(x_{cm_fut} + \bar{x}_{cm_ref} + \bar{x}_{cm_fut})) + \bar{x}_{cm_fut} - \bar{x}_{cm_ref} \quad (1)$$

205

206 Here F_{cm_ref} is the empirical cumulative distribution of the model over the reference period,
207 F_{obs}^{-1} the inverse cumulative distribution function of the observations, x_{cm_fut} the quantile that
208 is adjusted and \bar{x}_{cm_ref} and \bar{x}_{cm_fut} the means of the model output over the reference and
209 future periods. This mapping is applied over a rolling window of 9 years over the future period.

210

211 The approach ensures that not only the mean but also the shape of the distribution is corrected
212 without assuming a parametric form, whilst also preserving additive trends driven by the future
213 climate model. Furthermore ensures continuity between the historical and future period by
214 using a rolling window over the future period.

215

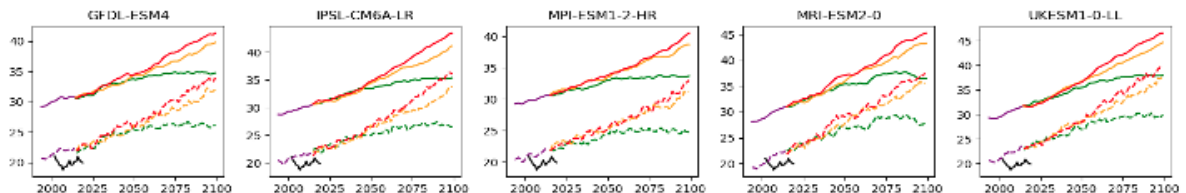
216 The results were evaluated in terms of the ability of the bias correction method to reduce the
217 model bias over the historical period, as well as preserve the trend between the future and
218 historical period. It was found that the method corrects the bias well over the historical period

219 for most regions, variables and gridcells in both the mean and 80th percentile at each grid cell.
 220 The trend between the future and historical period is well preserved in most regions and
 221 gridcells, with less than 0.1% of gridcells overall experiencing an absolute trend modification
 222 larger than 5%.

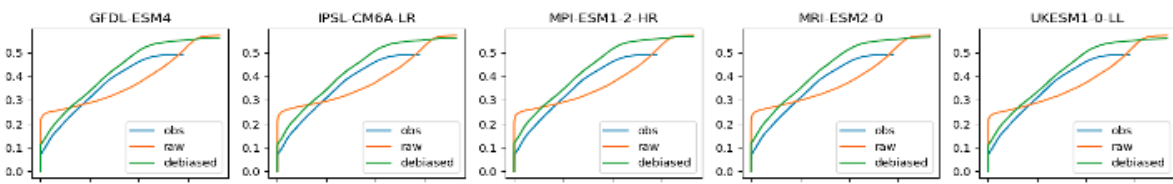
223
 224 To demonstrate the evaluation conducted, **Figure S24** shows the results for treecover over
 225 North-Western Canada. The plots for the remaining regions, including tree and no-tree cover,
 226 can be found in a notebook <https://github.com/jakobwes/State-of-Wildfires---Bias-Adjustment>.
 227 Investigating the timeseries of average treecover over the region, we find that the correction
 228 method reduces the bias over the historical period and matches the future period to the
 229 historical period (**Figure S24a**). The cumulative distribution functions of average tree cover
 230 merged over all spatial locations in observations and model match better after bias adjustment
 231 (**Figure S24b**). They do not match perfectly, and we note that this is a non-calibrated aspect
 232 that we do not expect to have zero bias but that is important to evaluate. Furthermore, we find
 233 that the improvement in both mean and 80th percentile hold across the region (**Figure 24c**).
 234 The trend between future and historical period is preserved for the majority of grid-cells, with
 235 the absolute change in trend being close to zero for most grid-cells.
 236

Evaluation of bias correction results for the JULES vegetation model over North-Western Canada

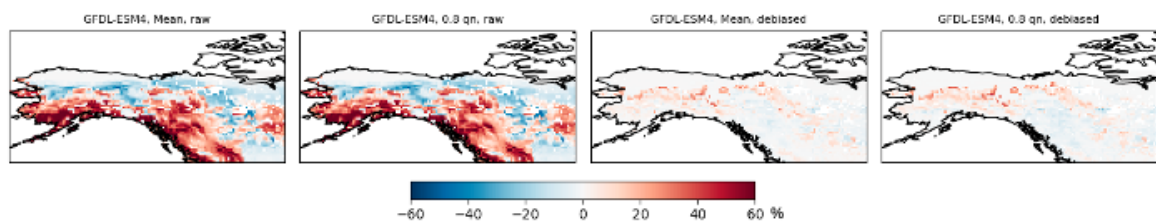
a) Timeseries of total tree cover of the area. MODIS VCF collection 6 in black. Raw model in solid lines, bias corrected model in dashed lines.



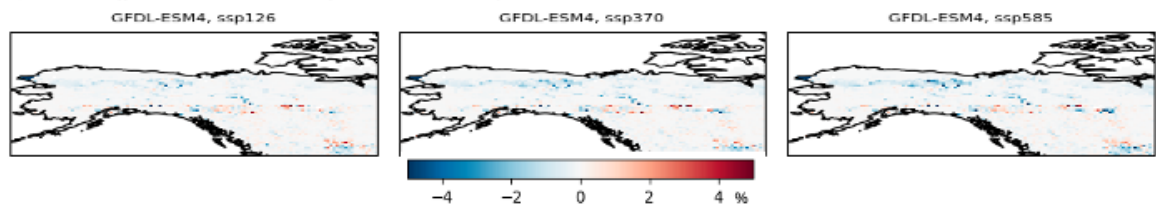
b) Cumulative distribution function across the region and historical time period.



c) Absolute model bias in mean and 80th percentile at each grid cells before (left two plots) and after (right two plots) bias correction.



d) Absolute difference in trend between future and historical period between raw and bias corrected model.



237
 238 **Figure S24:** Evaluation of the JULES vegetation model bias adjustment for tree cover over
 239 North-Western Canada. a) Timeseries of tree cover over the area for different climate models
 240 both with historical and scenario runs, raw model in solid lines, bias corrected models in

241 dashed lines and MODIS VCF in black. b) Cumulative distribution function of tree cover values
 242 across region and historical time period for different climate models for observations (blue),
 243 raw models (orange), debiased models (green). c) Absolute model bias in mean and 80th
 244 percentile for the GFDL-ESM4 climate model before (left two plots) and after bias adjustment
 245 (right two plots). d) Absolute difference in trend (difference between future and historical
 246 period) between raw and bias corrected GFDL-ESM4 model for ssp126, ssp370 and ssp585
 247 scenarios.

248
 249

250 **Modelling Frameworks**

251

252 **PoF**

253

254 The Probability of Fire (PoF) system uses gradient-boosted decision trees to provide a
 255 probability forecast of active fire occurrence (McNorton and Di Giuseppe, 2024). The
 256 supervised algorithm which trains an ensemble of decision trees uses regularization
 257 techniques to prevent overfitting [Chen & Guestrin, 2016]. The training, based on 2010-2014
 258 MODIS active fire detections, classifies a positive fire event as any detection within either a 1
 259 km or 9 km grid cell. The 9 km resolution is used for attribution due to cost, whereas the 1 km
 260 resolution provides high resolution forecasts which are displayed in the forecast maps
 261 provided here, in the supplementary material, but are not fully explored in this study.

262

263 The relative contribution of each input control to the model prediction is evaluated using
 264 Shapley values, computed using the Shapley Additive exPlanations python library [Lundberg
 265 & Lee, 2017]. The SHAP value indicates the importance of each feature in a model, where a
 266 positive SHAP value reflects a positive impact on the model prediction and a negative SHAP
 267 value reflects a negative impact. Specifically for this study we use the TreeExplainer, which
 268 computes the SHAP values by interrogating the structure of the decision trees within the model
 269 based on the input feature values. The probability controls are then normalised and grouped
 270 into the four categories given in **Table 3** of the main text. By combining these with the total
 271 amount of fires predicted for a given area we can attribute those fires into one of the four
 272 controls. The ‘Other’ control also includes fire occurrences not predicted by the model. This is
 273 computed given by:

274

$$275 \quad \textit{Other} = SHAP[\textit{Other}] + \max(0, \textit{Area_Total_Fires_Observed} \\ 276 \quad \quad \quad - \textit{Area_Total_Fires_Predicted}) \\ 277 \quad \quad \quad (2)$$

278

279 Where, SHAP[Other], is the contribution of the ‘Other’ control to the total predicted fires for a
 280 given region and, *Area_Total_Fires_Observed* and *Area_Total_Fires_Predicted* are the total
 281 number of observed and predicted fires for the same region.

282

283 **ConFire**

284

285 ConFire is a burned area attribution tool, used for trend detection and attribution (Kelley et al.,
 286 2019), event attribution (Kelley et al., 2021) and future projections (UNEP et al., 2022).
 287 ConFire finds the likelihood of causes of or changes in BA by optimising a simple, semi-
 288 empirical process representation model by applying Bayes Theorem. In our case, Bayes
 289 Theorem states that the likelihood of a model configuration described by a parameter set $\{\beta\}$
 290 and monthly explanatory variables (i.e model driving data) $\{X_{iv}\}$ given some training
 291 observation of monthly burned area fraction $\{Obs_i\}$ from MODIS MCD64A1, for cells i , is
 292 proportional to the prior probability of $\{\beta\}$ ($P(\{\beta\})$) multiplied by the probability of the
 293 observations given that model configuration:

$$294 \quad P(\{\beta\}|\{Obs_i\},\{X_{iv}\}) \propto P(\{\beta\}) \times P(\{Obs_i\} | \{X_v\}, \{\beta\}) \quad (3)$$

295
296
297
298

We use the zero-inflated logit distribution introduced by (Kelley et al., 2021) as our update distribution, as this is specifically designed to better represent the tails of the distribution during fire events:

299

$$P(\{Obs_i\} | \{X_{iv}\}, \{\beta\}) = \prod_i^N P(Obs_i | \{X_v\}_i, \{\beta\})$$

300

$$P(Obs_i = 0 | \{X_v\}_i, \{\beta\}) = (1 - M(\{X_v\}_i, \{\beta_M\})^{P_1}) \times (1 - P_0)$$

301

$$P(Obs_i > 0 | \{X_v\}_i, \{\beta\})$$

302

$$= (1 - P(Obs_i = 0 | \{\beta\})) \times \mathfrak{N}(\text{logit}(Obs_i) - \text{logit}(M(\{X_v\}_i, \{\beta_M\})), \sigma)$$

303

(4)

304

305

where $\{\beta_M\}$ is the set of parameters related solely to the underlying model, M , $\text{logit}(x) = \log\left(\frac{x}{1-x}\right)$, P_0 , P_1 and σ are parameters within the full set $\{\beta\}$ which describe the model error and $\mathfrak{N}(\mu, sd)$ is a normal distribution with mean of μ and standard deviation of sd .

308

309

The model, M , simulates fractional BA (fraction) via a number of controls. For attribution and outlook, these controls follow (Kelley et al., 2021; Burton et al., 2019): Fuel load, fuel moisture, ignitions and suppressions. This follows the general model structure of global fire models (Hantson et al., 2016; Rabin et al., 2017) and is most appropriate for looking at long term, coarse fire drivers (Moritz et al., 2005). For driver assessment, we separate out an additional control for “fire weather” and introduce a “snow cover” control. Model BA is the product of these controls, c :

316

$$M(\{X_v\}, \{\beta_M\}) = F_{max} \times \prod_c f(\{X_c\}, \{\beta_c\}) \quad (5)$$

318

319

Where F_{max} describes maximum monthly burned area fraction and is an optimizable parameter in set $\{\beta_M\}$, $\{X_c\}$ are the BA driving variables, $\{\beta_c\}$ the parameters related to control c and f is the function that describes the control influence on BA. Each control describes the expected BA if all other controls imposed no limitation on burning - for example, when c is fuel, $f(\{X_c\}, \{\beta_c\})$ describes the BA in perfectly dry conditions with saturated ignitions and no suppression. To achieve this, f is the logical function:

325

$$f(\{X_c\}, \{\beta_c\}) = 1 / \left(1 - \exp(-\beta_{c,0} - \sum_j \beta_{c,j} \times X_j)\right) \quad (6)$$

327

328

329

where $\beta_{c,j}$ is the contribution of driving variable X_j to the control and $-\beta_{c,0}$ is a parameter that can shift the midpoint of the sigmoid curve.

331

332

All variables X_v where normalised to be between $[0, 1]$ based on the training data to aid priors selection and optimization - though analytically this should have no impact on our results. Our priors fix the direction each drive can influence a control (drivers and direction are listed in Table 3 and 5) but beyond this relatively uninformed. Priors for $\beta_{c,j}$ where described by a log-normal distribution with a μ of 0 and σ of 10, and set to be positive for liberative drivers (one that increases the strength of a control) and negative for suppressive (ones that reduce the strength of a control). $\beta_{c,0}$ priors were set to a normal distribution with a mean of 0.5 and a standard deviation of 1. F_{max} and P_0 priors were set as a uniform distribution between 0 and 1 σ was set to a half-normal with mean of 0 and standard deviation of 10.

340

341

342

We sampled the posterior distribution using Bayesian inference following a similar protocol to (Barbosa, 2024) with the pymc python package version 5 (Abril-Pla et al., 2023), employing 100 chains each over 1000 warm-up iterations (that were not subsequently used) and 100 sample iterations using the No-U-Turns Hamilton Monte Carlo sampler (Hoffman

345

346 and Gelman, 2011) while utilising 50 % of the data or a minimum of 6000 grid cells. To
 347 sample the posterior distribution, we then randomly sample 50 iterations from each chain,
 348 thereby approximating the posterior with 1000 ensemble members. As per (Barbosa, 2024),
 349 for evaluation (**Figure S28-S39**) we trained the first half of the period and tested on the
 350 second half. For the rest of the results, we trained on the full period.

351
 352 We obtaining probability distributions from the model posterior for our results, ConFire offers
 353 two probability, which we have adapted slightly from (Kelley et al., 2021) :

- 354
 355 1. The likelihood of different levels of burning for a specific event (i.e a grid cell in a
 356 given timestep) which considers uncertainty explained by the model and residual
 357 uncertainty described by our error parameter, σ . We use this when we are
 358 comparing a single grid of cells and months, such as for evaluation, and for
 359 assessing the un. The likelihood of a Burned Area, BA , under drivers, X , which can
 360 be out-of-training sample, is:

$$361 \quad P(BA | (X_v, \beta | \{Obs_i\}, \{X_{iv}\})) = \int_{\beta} P(\beta | \{Obs_i\}, \{X_{iv}\}) \times P(BA | \beta) d\beta \quad (7)$$

362
 363 Where $P(BA | \beta)$ is take from equation 4.

364
 365 When building distributions for multiple grid cells or time periods, as with building a
 366 climatology in **Section 3.3**, we convolute the probability distributions of individual
 367 time periods and cells following equations in (Kelley et al., 2021). Converting
 368 probabilities over a large number of cells gives us the second measure.

- 369
 370
 371 2. The emergent probability of different mean levels of BA over many events explained
 372 directly by the model and its driving variables. We use this when assessing the
 373 emergent likelihood of burning in **Section 3.4** and **Section 3.5**. This is the same as
 374 taking the mean of n simulations in equation 7 as n tends to infinity. Doing this,
 375 $P(\{Obs_i\} | \{X_{iv}\}, \{\beta\})$ from equation 4 will tend towards a BA of model M output
 376 weighted by the likelihood of a zero BA:

$$377 \quad D(BA) = \lim_{n \rightarrow \infty} \left[\sum_{i=1}^n P(BA | (X_v, \beta | \{Obs_i\}, \{X_{iv}\})) / n \right]$$

$$378 \quad = \int_{\beta} M(\{X_v\}_i, \{\beta_M\}) \times (1 - M(\{X_v\}_i, \{\beta_M\})^2) \times (1 - P_0) d\beta \quad (8)$$

381
 382 For attribution and future projections, ConFire produces correctly ranked by consistently
 383 biased probability distributions (**Supplement Section “Change in Likelihood of High
 384 Burned Area in 2023 due to Total Climate Forcing and Socioeconomic factors”**). The
 385 final step is therefore to introduce a correction factor. As this distribution bias is constant
 386 across the observed BA distribution, a simple scaling factor is all that's needed. To do this,
 387 we assign the likelihood associated with the BA in equation 8 with a scaled burned area
 388 (BA^*) so that the mean of the sample distribution matches the mean of the observation for
 389 the period 2003-2019.

$$390 \quad BA^* = BA \times \Sigma(\{Obs_i\} / \int_0^1 D(BA) \times BA dBA \quad (9)$$

391
 392 BA^* is then used in equation 8.

393 394 **Attributing Fire Weather**

395

396 Bias Correction

397 We evaluated the individual variables in the FWI (see evaluation), and found that each variable
398 was slightly biased compared to ERA5 reanalysis. We therefore applied a bias correction to
399 the final FWI, rather than bias-correcting each individual variable.

400
401 We bias-corrected the HadGEM3 2023 large ensemble based on a bias assessment of the 15
402 historical members from 1960-2013 vs. ERA5 observation-driven FWI, using a simple linear
403 regression on fwi transformed using:

$$405 \quad fwi_* = \log(\exp(fwi) - 1) \quad (10)$$

406 to remove the physical bound at 0. We use this instead of using a straight \log transformation
407 as it ensures numerical stability at higher values, crucial when dealing with extreme FWI
408 values, thereby avoiding blow-up effects. It also preserves the extreme tail of the FWI
409 distribution, allowing us to accurately capture and analyse critical events associated with high
410 fire risk..

411
412 We perform a simple linear regression on ERA5 and on each historical member to obtain the
413 basic regression parameters:

$$414 \quad fwi_* \sim fwi_{*,0} + \Delta_{fwi} \times t \quad (11)$$

415 Where t is time, and $t = 0$ is set to 2023, Δ_{fwi} is the rate of change, or trend, of fwi_* and $fwi_{*,0}$
416 is the estimated fwi_* for 2023. Our bias correction is therefore based on present-day levels of
417 warming, taking account of the additional warming from 2013-2023 (assuming the trend from
418 1960-2013 continues to 2023 linearly). If anything this is likely conservative given that warming
419 rates may have increased more rapidly in the last 10 years.

420
421 We generate the bias-corrected 2023 ensemble by correcting each of the 525 present-day
422 ensemble members against each of the 15 historical members (creating an ensemble of 7875
423 members). Due to the perturbation procedure used to generate the 2023 ensemble from the
424 historic (Ciavarella et al., 2018), we can not assume that present-day members pair to
425 historical members. We therefore iterate over all possible pairs:

$$427 \quad fwi_{*,corrected} = \left\{ fwi_{*,0,ERA5} + (fwi_{*,i} - fwi_{*,0,j}) \times \sigma_{\Delta}(fwi_{*,j}) \frac{\sigma_{\Delta}(fwi_{*,i})}{\sigma_{\Delta}(fwi_{*,ERA5})} \right\} \quad (12)$$

$$428 \quad \sigma_{\Delta}(fwi_*) = sdev(fwi_* - \Delta_{fwi} \times t)$$

429 Where i is a present-day ensemble member, and j is a historical member.

430
431 We finish by applying the inverse of the transformation from equation 10 :

$$432 \quad fwi_{corrected} = \log(\exp(fwi_{*,corrected}) + 1) \quad (13)$$

433

434 Probability Ratio

435 We use the ERA5 2023 FWI for our event threshold in each region, using the month of peak
436 anomaly from **Figure S2** in each region. We use this threshold to calculate the probability ratio
437 (PR) of the event occurring with and without climate change. To calculate the PR, we find the
438 number of ensemble members that exceed the 2023 ERA5 FWI value in the bias-corrected
439 ALL simulation, and divide this by the number of members that exceed the same value in the
440 bias-corrected NAT simulation, bootstrapping 10,000 times to giving the probability of
441 exceeding the observed 2023 FWI value in a world with and without climate change plus
442 uncertainty bound for the 5-95th percentile.

$$443 \quad PR = p(\text{ALL}) / p(\text{NAT})$$

444

445 **FireMIP**

446

447 For the multi-model ensemble we use simulations from the ISIMIP3a fire sector, as published
448 in (Burton & Lampe et al. 2023). The 7 models reporting BA for ISIMIP3a are shown in the
449 table below. The methodology follows the ISIMIP3a Impacts Attribution protocol, as outlined
450 in (Mengel et al., 2021), where the factual historical simulations are driven with GSWP3-W5E5
451 reanalysis data, and the counterfactual simulations are the same historical data which has
452 been detrended via quantile mapping (Mengel et al., 2021).

453

454 As outlined in (Hantson et al., 2016), the spread in the absolute BA is large amongst the
455 observations, models and regions and therefore a normalised relative anomaly (RA) rather
456 than absolute BA is used for the analysis. To calculate the RA in present day BA, we subtract
457 the counterfactual mean, and divide by the counterfactual mean. By comparing both factual
458 and counterfactual experiments to the counterfactual mean, we are looking at the fractional
459 increase in BA driven by climate change compared to a baseline without climate change.
460 Based on model performance by AR6 region, a region-specific weighting is also applied. The
461 weighting is based on the model's distance to the observed BA temporal RA using both
462 FireCCI5.1 and GFED5. To measure the uncertainty, random noise is generated and scaled
463 by the climatological RMSE of each model. This noise is then added to the modelled relative
464 anomaly, this process is repeated 1000 times. Then, bootstrapping is applied to the monthly
465 regional BA RA (now with noise added in) according to the weight for each model. Uncertainty
466 is calculated by taking the 2.5-97.5th percentile of the resultant histogram. All results are
467 reported as P50 [P2.5, P97.5]. The methods are explained in full in (Burton & Lampe et al.
468 2023).

Table S1: FireMIP Models used for attributing median burned area. Table reproduced from (Burton & Lampe et al. 2023)

Model		CLASSIC	INFERNO	LPJ-GUESS-SIMFIRE-BLAZE	LPJ-GUESS-SPITFIRE	ORCHIDEE-MICT-SPITFIRE	SSiB4/TRIFFID	VISIT
Fire Model		CLASSIC	INFERNO	SIMFIRE	SPITFIRE	SPITFIRE	Li	After (Thonicke et al., 2001)
Land / Vegetation		CLASSIC	JULES	LPJ-GUESS	LPJ-GUESS	ORCHIDEE	SSiB	VISIT
Dynamic Veg	Physiology	Yes	Yes, via TRIFFID	Yes	Yes	Yes	Yes, via TRIFFID	Yes
	LAI	Yes	Yes, via TRIFFID	Yes	Yes	Yes	Yes	Yes
	Bio-geography	No	Yes, via TRIFFID	Yes	Yes	Yes	Yes	No
Nitrogen Cycle		Yes	Yes	Yes	Yes	No	Yes	Yes, but C-N coupling is limited
No. PFTs		9	13	17	17	19	7	33 (biome types)
No. Soil Layers		20	4	2	2	11	3	2
Fuel		Vegetation and litter	Vegetation & top soil layer as proxy for litter	Vegetation, litter	Litter	Vegetation and litter	Vegetation and litter	Litter
Ignitions	Natural	Prescribed lightning	Prescribed lightning	SIMFIRE describes annual BA + fire-climatology -> daily BA used as Fire-Probability	Prescribed lightning	Prescribed lightning	Prescribed lightning	Probabilistic based on fuel wetness

	Anthropogenic	Prescribed population density	Prescribed Population density	SIMFIRE includes suppression by humans	Prescribed population density	Prescribed population density	Prescribed population density	No
Suppression		Prescribed population density	Crops, population density	Crops (100%), prescribed population density (Hyde3.1)	Crops, population density	Prescribed population density, crops	Prescribed population density and GDP	Low fuel load
Spread		Wind speed and soil moisture	None	Daily BA (no explicit spread)	Rothermel equations including wind speed, tree fraction, grass fraction, fuel moisture, fuel load and characteristics	wind speed, tree fraction, grass fraction, fuel moisture, fuel load	Wind speed and soil moisture	None
Model inputs		SW & LW radiation, precipitation, air temperature, specific humidity, wind speed, atmospheric pressure, population density, lightning	SW & LW radiation, precipitation, air temperature, specific humidity, wind speed, population density, lightning	SW radiation, precipitation, air temperature (mean, min, max), relative humidity, wind speed	SW radiation, precipitation, air temperature, specific humidity, wind speed, atmospheric pressure, population density, lightning	SW & LW radiation, precipitation, air temperature, specific humidity, wind speed, atmospheric pressure, PFT map, population density	SW & LW radiation, precipitation, air temperature, specific humidity, wind speed, atmospheric pressure, population density, and GDP, peat map, land cover change	Air temperature, precipitation, air vapor pressure, cloudiness, wind
Resolution		1 deg	0.5 deg	0.5 deg	0.5 deg	0.5 deg	0.5 deg	0.5 deg
References		(Melton et al., 2020)	(Burton et al., 2019, 2020; Mangeon et al., 2016)	(Rabin et al., 2017; Smith et al., 2014; Knorr et al., 2014)	(Rabin et al., 2017; Smith et al., 2014; Thonicke et al., 2010; Lehsten et al., 2009)	(Yue et al., 2014, 2015)	(Huang et al., 2021, 2020; Li et al., 2012; Hugelius et al., 2013; Li et al., 2013)	(Ito, 2019)

471

472

473 Evaluation

474 *POF*

475

476 The PoF model, trained on observed fire activity, provides a daily probability of fire occurrence
477 based on the input variables described in **Table 3** of the main text. The three cases explored
478 in the main study can be visualised as fire risk maps at a 1 km resolution, higher than the 9
479 km used for attribution. The 1km predictions show that whilst PoF often fails to capture the
480 true total number of active fires, the relative attribution is likely to be accurate given by the
481 models ability to capture the spatiotemporal pattern of fire activity reflected by the forecast
482 danger shown in the figures below. Of the three case studies the model accurately reflects fire
483 activity for Canada and Western Amazonia, and whilst high fire danger is modelled over
484 Alexandroupolis, Greece, it fails to capture the severity of the event.

485

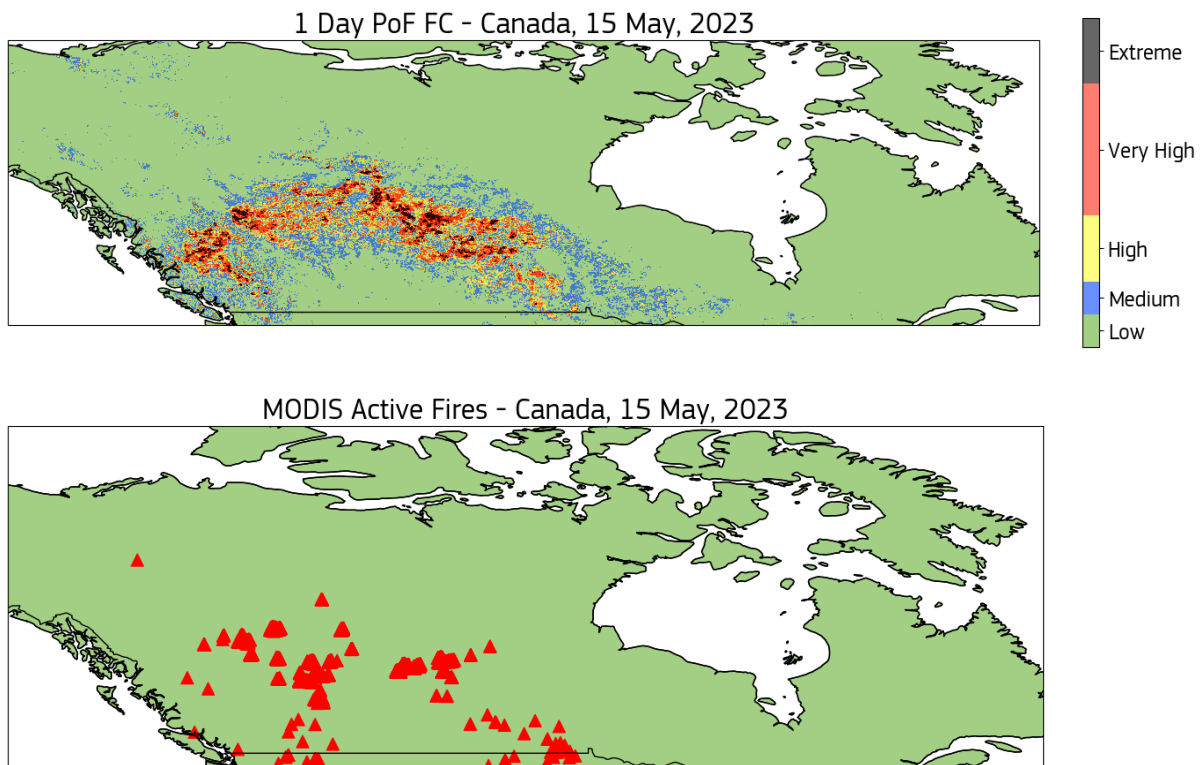
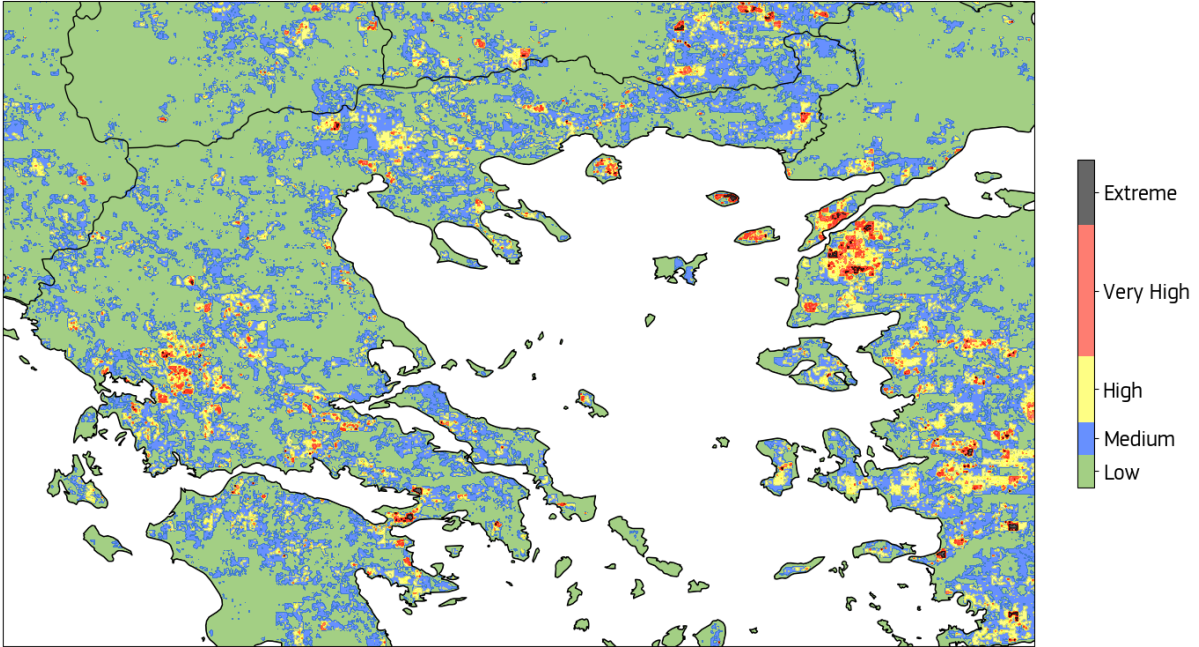


Figure S25: Spatial representation of the day 1 PoF forecast at ~1km resolution expressed as a danger rating for the 15th May over Canada (top). MODIS active fire detections for the same day and domain (bottom).

1 Day PoF FC - Greece, 21 August, 2023



492

MODIS Active Fires - Greece, 21 August, 2023



493

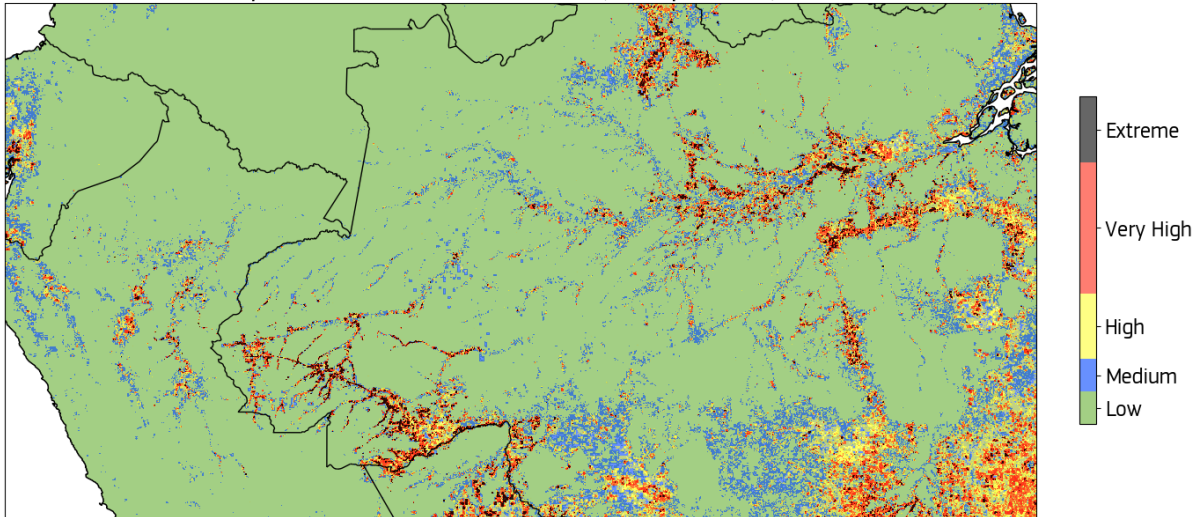
494

495

496

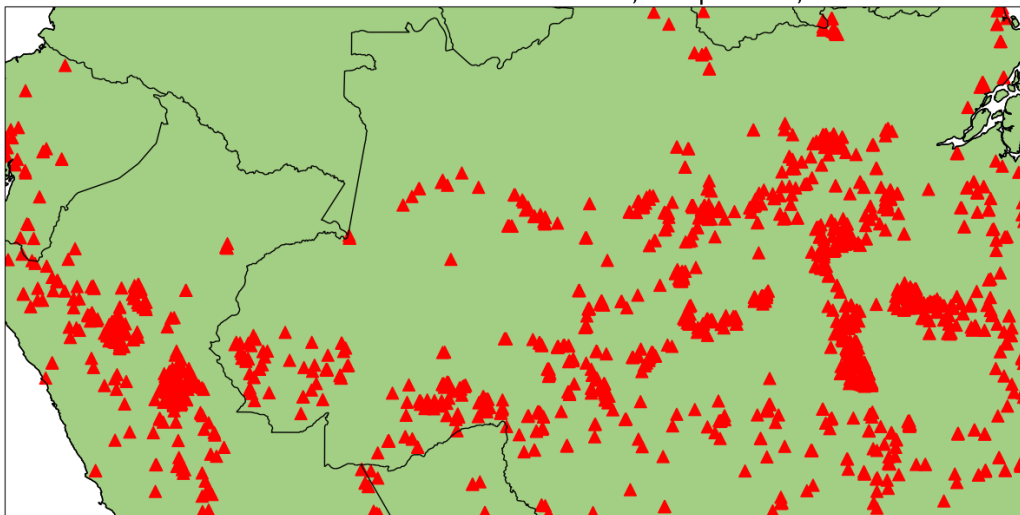
Figure S26: Spatial representation of the day 1 PoF forecast at ~1km resolution expressed as a danger rating for the 21st August over Northern Greece (top). MODIS active fire detections for the same day and domain (bottom).

1 Day PoF FC - Western Amazonia, 9 September, 2023



497

MODIS Active Fires - Western Amazonia, 9 September, 2023



498

499

500

501

502

503

504

505

Figure S27: Spatial representation of the day 1 PoF forecast at ~1km resolution expressed as a danger rating for the 9th September over Western Amazonia (top). MODIS active fire detections for the same day and domain (bottom).

ConFire

506

507

508

509

510

511

512

513

514

515

516

The ConFire model simulates a probability distribution of BA which, unlike most numerical or ensemble-based models, requires a probabilistic technique for evaluation.

The uncertainty range of the ConFire is crucial for the analysis in this study. We obtain confidence in our results by seeing if the shift of the model's probability distributions is significant compared to the size of the uncertainty of that distribution. Suppose the uncertainty range is larger than any change when testing for i.e, attributing with or without climate change, future changes, or seasonal anomaly. In that case, the framework will tell us, and our results will show that these are unlikely/not significant. Conversely, if the change in distribution is larger than the model's uncertainty range, we can make a confident statement even if that model is uncertain.

517 As the precision of the modeling framework is inherent in the analysis itself, the main aspect
518 to evaluate is the ability of the model's probability distribution to represent the range of
519 uncertainties when tested against observations accurately. To do this, we followed the
520 evaluation procedure outlined in (Barbosa, 2024), which we summarise here.

521

522 We trained the model during the first half of each period used in the analysis and performed
523 subsequent evaluations on the second half. The training period for near-real-time driver
524 assessment was 2014-2018, and for the attribution/future projections run, 2003-2011. The
525 evaluation period was 2019-2023 for driver assessment and 2012-2019 for attribution/future
526 projections. Using a different period from the optimization ensures an independent model
527 evaluation and provides an indication of how well the framework captures uncertainty in out-
528 of-temporal sample observations.

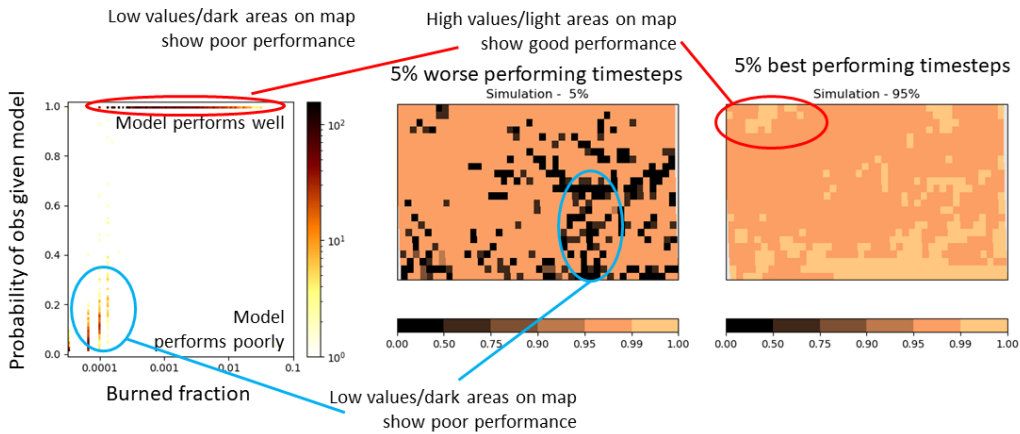
529

530 The FLAME system (Barbosa, 2024) that we merge with ConFire automatically generates a
531 series of evaluations which we show for region region in turn in the subsequent two sections.
532 While the techniques are outlined in (Barbosa, 2024), these automated figures have not
533 previously been published. So alongside the evaluation procedure below is a guide to interpret
534 if these plots show a good model performance.

535

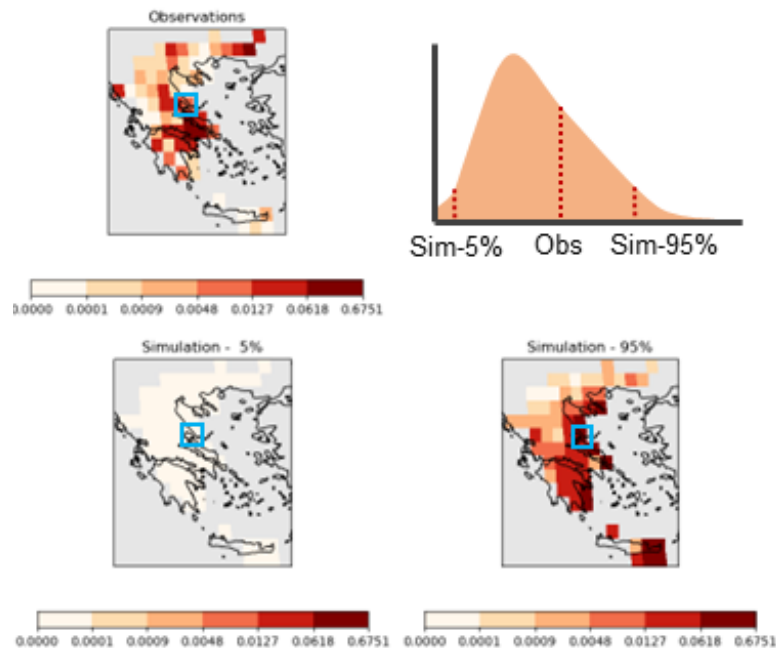
536 For the evaluation period, we assess how well the model predicts new observations by testing
537 how likely the observations are given the optimized model (equation 7). While this sounds
538 counter-intuitive, we do this rather than test the model given the observations because the
539 model doesn't yield a single answer or a set of numbers, but rather a distribution of model
540 parameters and output, reflecting inherent uncertainty in the processes. This approach allows
541 for comprehensive testing of the entire model's posterior probability distribution at once and
542 provides insight into the model's ability to generate the observed distribution and capture the
543 uncertainty in the modeled process. We approximate the probability of an observation given
544 our model by sampling 10 parameter ensemble members from each of our 100 chains,
545 providing us with 1000 ensemble members, and sample the likelihood as per (Kelley et al.,
546 2021). The example below, taken from **Figure S32**, shows how we summarise this for each
547 observation (scatter plot left) and all observations in a time series for each cell (middle and
548 right). If the model performed perfectly, the probability of the observations given the model will
549 all be close to 1, as the scatter plot indicated for BA fractions above ~ 0.0003 . The model won't
550 always capture the uncertainty required to generate the observations. This generally happens
551 at specific burned areas (like low ones in this example). Areas where this happens often are
552 highlighted on the map with the map in the middle showing the performance at the 5th
553 percentile of the time series.

554



555
556
557

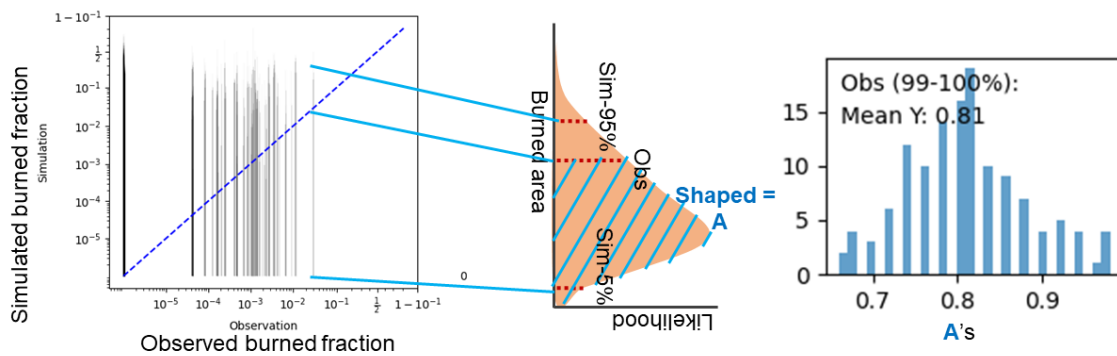
558 We also determine the percentile of our observations within the model's posterior probability
559 distribution. In an unbiased model, we expect the observation's position to be random. We can
560 start by doing this visually, as shown in the example from **Figure S30**: Observational BA (top
561 left) should generally fall between the two simulation maps (bottom) that span the 5-95
562 percentile of the model distribution. Taking the cell highlighted in blue for example - the lower
563 model estimate is close to zero and the upper is higher than the observations, indicating a
564 good performance at capturing the observations. Evaluating include parameters representing
565 noise or stochasticity in the system, that is not always included in the main analysis. Given the
566 inherent randomness in fire in our study regions, this does result in very broad BA distributions
567 in the model so a larger difference between the maps showing the BA in the model's tails
568 ("simulation - 5%" and "simulation - 95%") is to be expected.



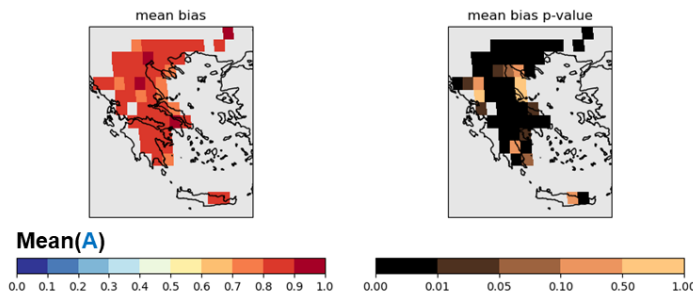
569
570
571
572

We compare the observations (x-axis) likely range (5-95 percentile) of the model's probability distribution. Similarly to the maps above, if the model captures the uncertainties, the

573 observations should fall within this range - i.e the 1:1 line should fall inside the span of the
 574 model, as seen in this example from **Figure S36**. We also calculate the mean position of the
 575 observations. This is simply the probability of BA greater than the observation, calculated by
 576 integrating equation 7 for BAs in the range $[0, BA]$. For simulations used in attribution, we also
 577 build histograms (right, taken from **Figure S39**) of this bias across different percentiles of the
 578 observations. This shows us if there is any part of the distribution that has a substantially
 579 different bias. In an unbiased model, these observational positions in the framework's
 580 probability distribution should average ("Mean Y:" in the histogram) to 0.5. Numbers close to
 581 1 indicate the observations on average tend towards the higher BA in the distribution, and the
 582 model generally underestimates BA. This alone does not show if the model performs poorly,
 583 and a consistent bias across all parts of the BA distribution indicates correct ranking, though
 584 the need for scaling for attribution analysis (see **Supplement Section "Modelling
 585 Frameworks > Confire"**).
 586



587
 588 We also map out the mean position of the observations of the times series. Again, in an
 589 unbiased model, given enough timestep, this should average out to 0.5 for each gridcell.
 590 However, given the small number of timesteps, we map is the observational position in the
 591 frameworks posterior tends to be significantly different to 0.5 using a t-test to calculate a p-
 592 value for if the mean of the posterior position of the monthly observations for a given grid cell
 593 is significantly different from 0.5. Low p-values indicate where the model is biased, which tends
 594 to suggest too low or high burning.
 595



596
 597
 598
 599
 600 **Drivers of Regional Burned Area Extremes**
 601
 602 The model has shown a consistent ability to capture observations within its uncertainty range
 603 across all regions, indicating a robust representation of uncertainty. It also demonstrates a

604 high likelihood of aligning with actual observations, indicating strong alignment between
605 model outputs and real-world data. It effectively represents BA anomalies based on the
606 driving variables, demonstrating strong explanatory power across different regions.

607

608 However, the model consistently exhibits a low bias in estimating BA across regions, often
609 underestimating the BA, particularly in specific high-burn regions such as deforestation
610 areas in Western Amazonia and patches of high BA in northern Canada. This highlights the
611 common need across regions for better integration of data on human influences and
612 interactions with fire. It may also hint at the need for better representation of non-linearity
613 between drivers and BA.

614

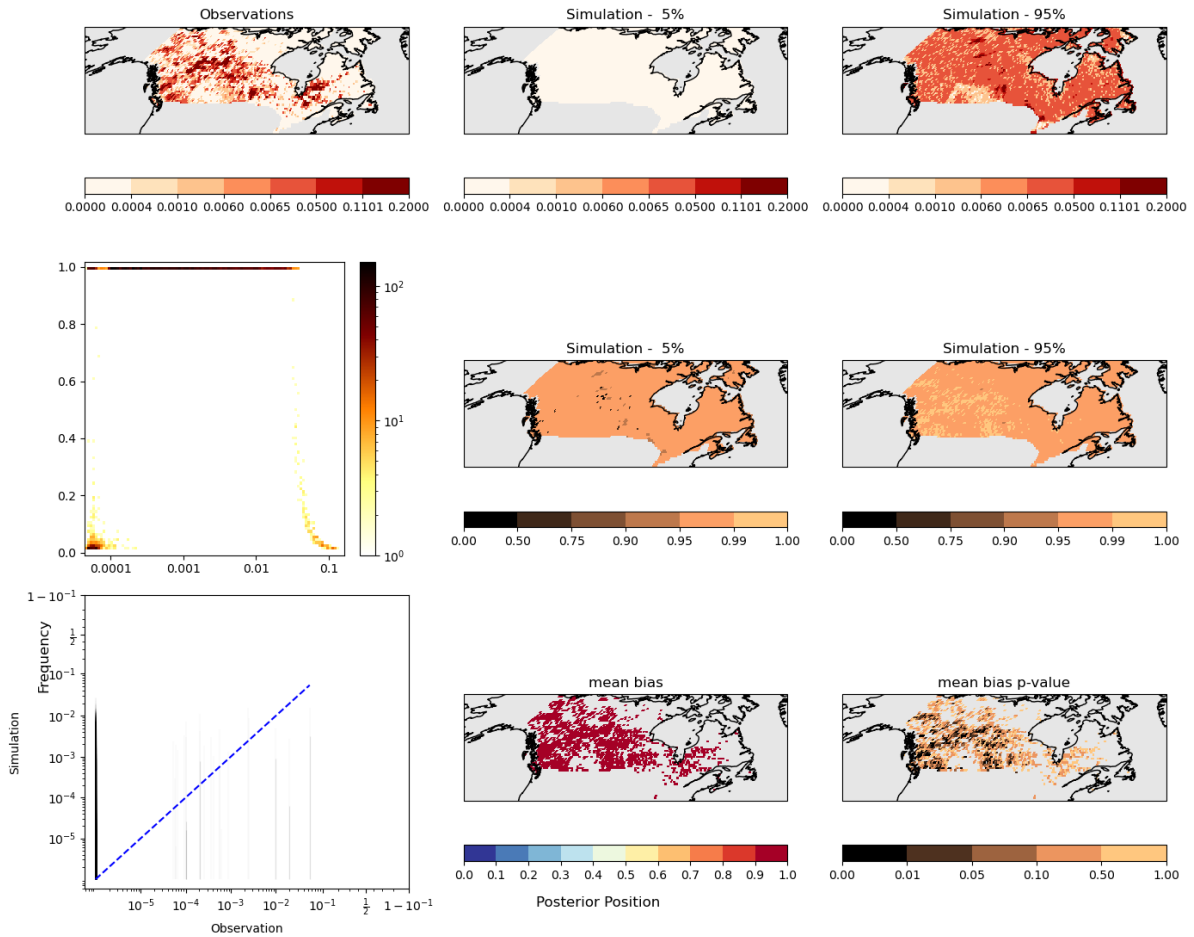
615

616 **Canada**

617 Our evaluation indicates that the model's assessment of uncertainty does a reasonable job
618 of capturing the observational range, particularly for high BA. The top row of **Figure S28**
619 demonstrates this - the observed (on the left) falls between the 5-95% range of the model.
620 However, there are patches of high BA that are slightly farther north than in the
621 observations. The model accurately identifies low burning in agricultural regions in southern
622 Saskatchewan and Alberta, and it suggests lower burning in the north while still
623 acknowledging the possibility of some burning.

624

625 The probability of observations given the model is very high, especially for medium to high
626 BA ranging from 0.03% to 3% (**Figure S28** left middle row). This demonstrates that the
627 modelling framework does a reasonable job of generating observations within this
628 range. Except for a few locations, even the worst performances tend to show a likelihood of
629 observations given a model of > 0.95 . For very high BA, the probability decreases but
630 generally falls within the model's uncertainty range (bottom left), and ranked indicating that
631 the model can effectively identify high burning anomalies. However, it tends to
632 underestimate the increase in BA during such anomalies (i.e in **Figure 14**). In fact, the model
633 tends to be biased towards slightly lower BA in many regions of Canada (bottom middle
634 map), though only significantly so in the South and West of the country (bottom left map).
635 Interestingly, the BA picked up by the driving variables alone also effectively reproduces
636 spatial patterns of BA and regions of high anomalies in 2023, suggesting that the driving
637 variables used are good at explaining the observed patterns in BA.



638

639

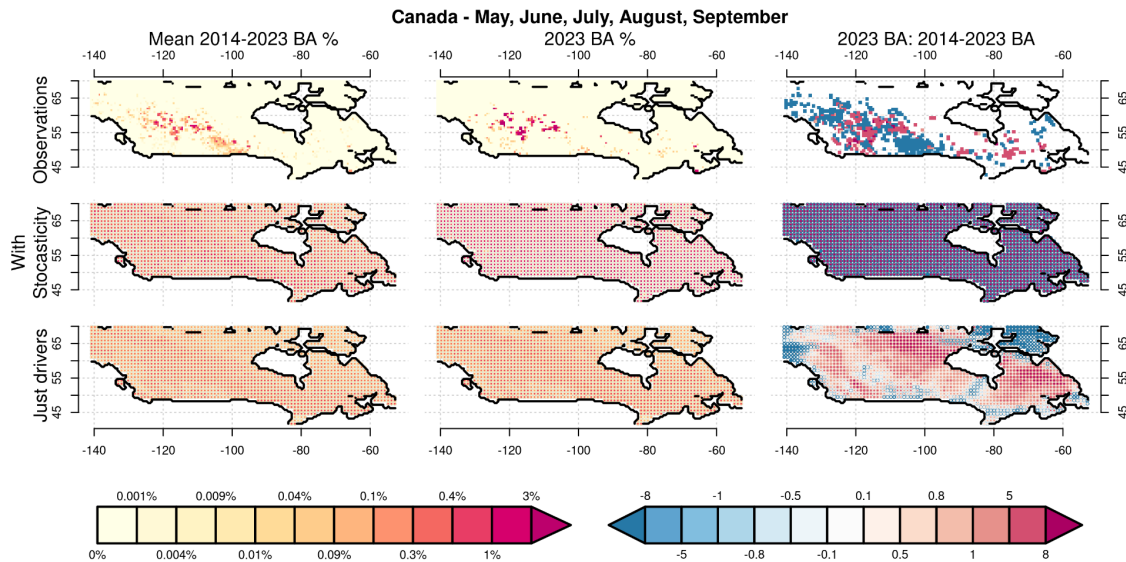
640

641

642

643

Figure S28: Evaluation plot for driver attribution configuration in **Section 3.3** over Canada. (top row) observed and simulated BA fraction (%). (Middle row) the likelihood of the out-of-sample observations given the models probability distribution and (bottom row) observations position in the model distribution. See top of this section for interpretation guide.



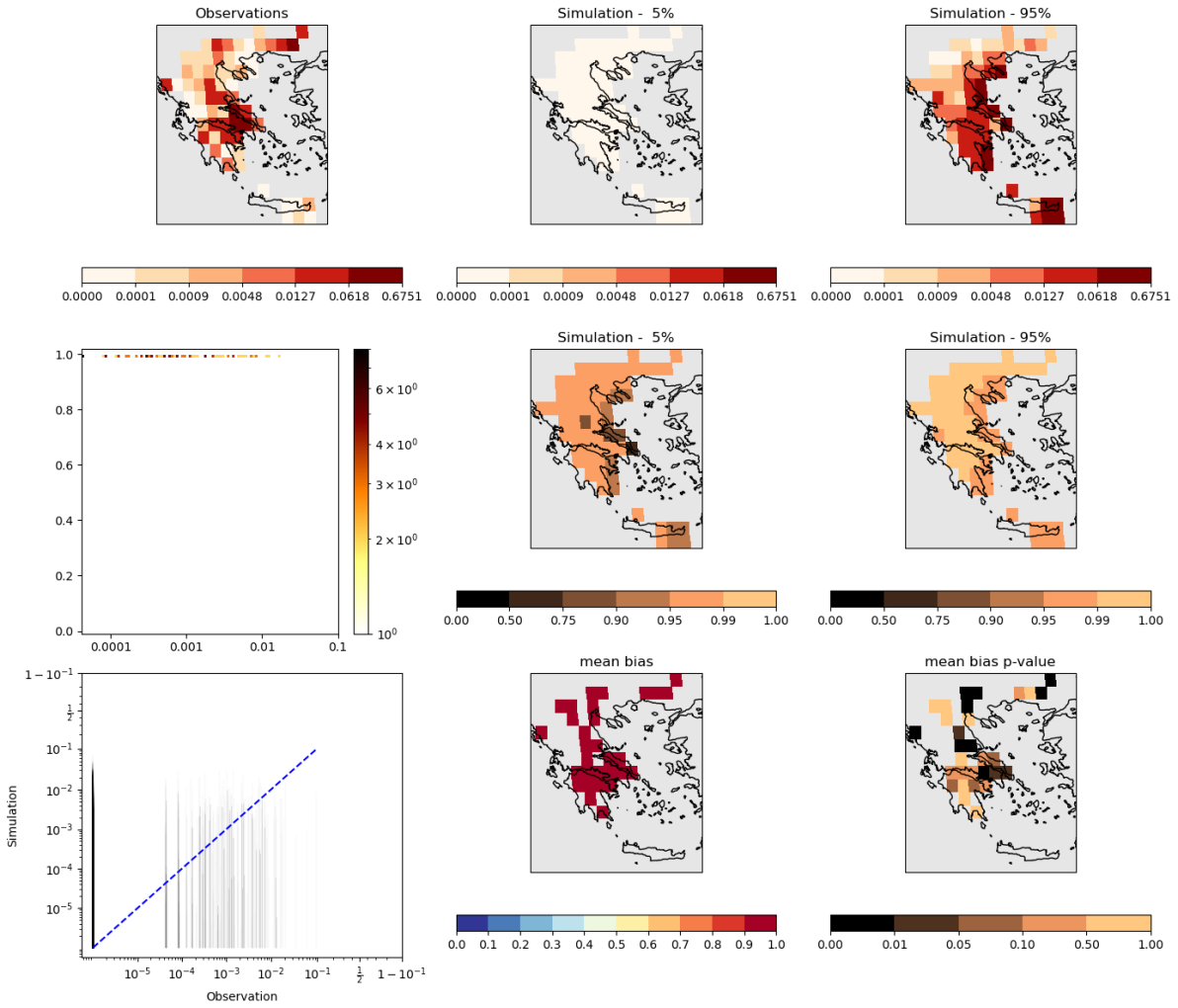
644

645 **Figure S29:** BA % over Canada for May-September for driver attribution configuration in
 646 **section 3.3** over (left) 2014-2023 (middle) 2023 and (right) for 2023 anomaly compared to
 647 2014-2023, expressed as a factor of increase (red) or fractional decrease (blue). The top row
 648 is observations, the middle row in ConFire includes stochasticity (equation 7) and the bottom,
 649 just considers the influence of drivers (equation 8). For ConFire, the size of the dot in each
 650 grid cell shows the likelihood (larger = higher likelihood) of a BA fraction (or BA change) being
 651 greater than a given threshold (where the threshold is represented as a coloured dot, see
 652 legend at the base). High BA overlap smaller. i.e on the left, a large pale orange dot indicates
 653 a high likelihood of annual average BA exceeding 0.1%, with a small dark red dot indicating a
 654 small but non-zero likelihood of exceeding 3%

655

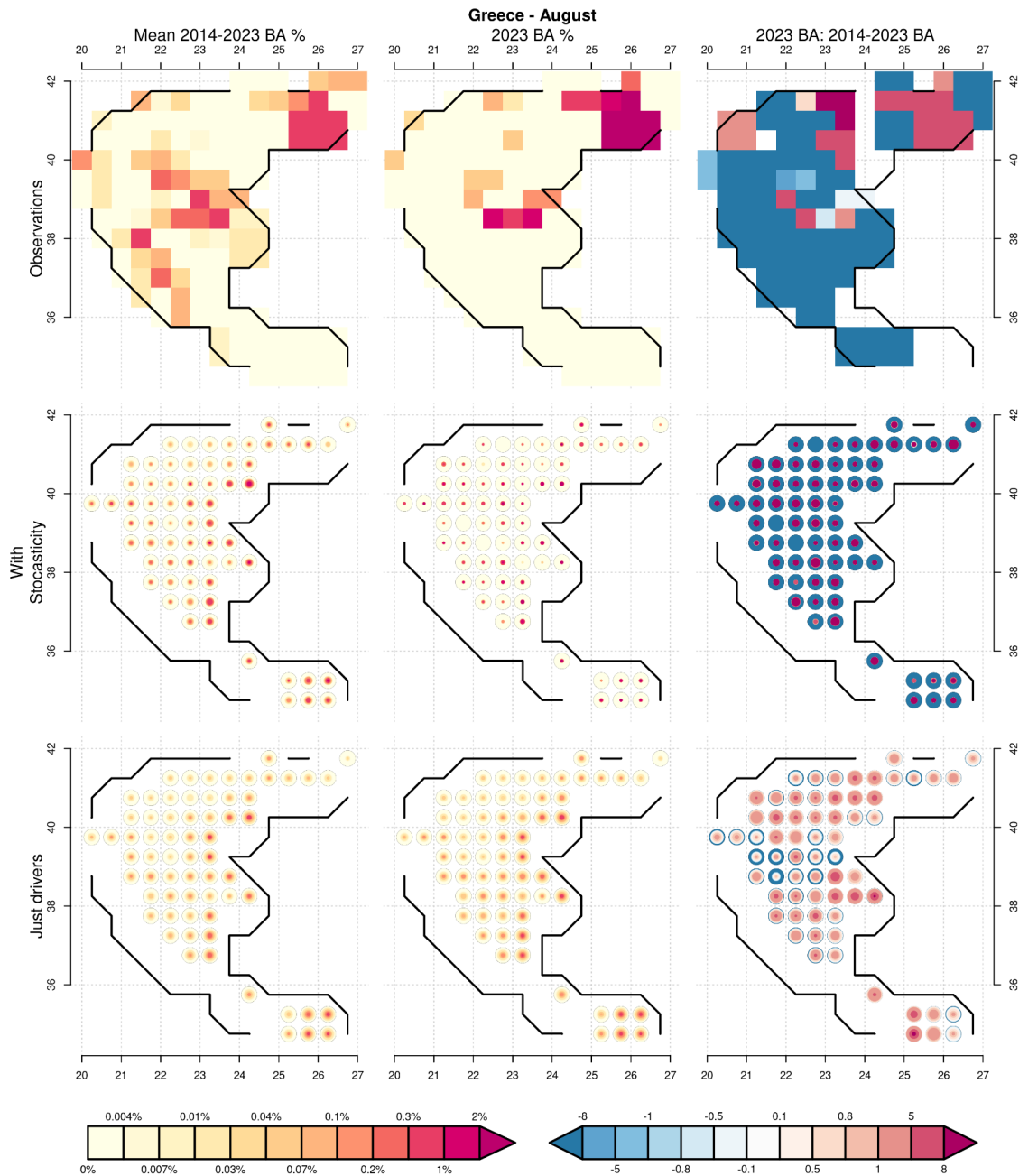
656 **Greece**

657 The model effectively represents uncertainties surrounding observed BA and accurately
 658 captures the gradient between low burning in the northwest of Greece and high burning
 659 around the southeastern coast. The model's observations show extremely high likelihood
 660 across all BA, with only a slight dip to around 0.75 likelihood in a few months in coastal
 661 Thessaly. Additionally, there is a consistent pattern of underestimating BA across all areas of
 662 Greece, although this is only significant in a few places.



663
664
665

Figure S30: same as **Figure S28** for Greece



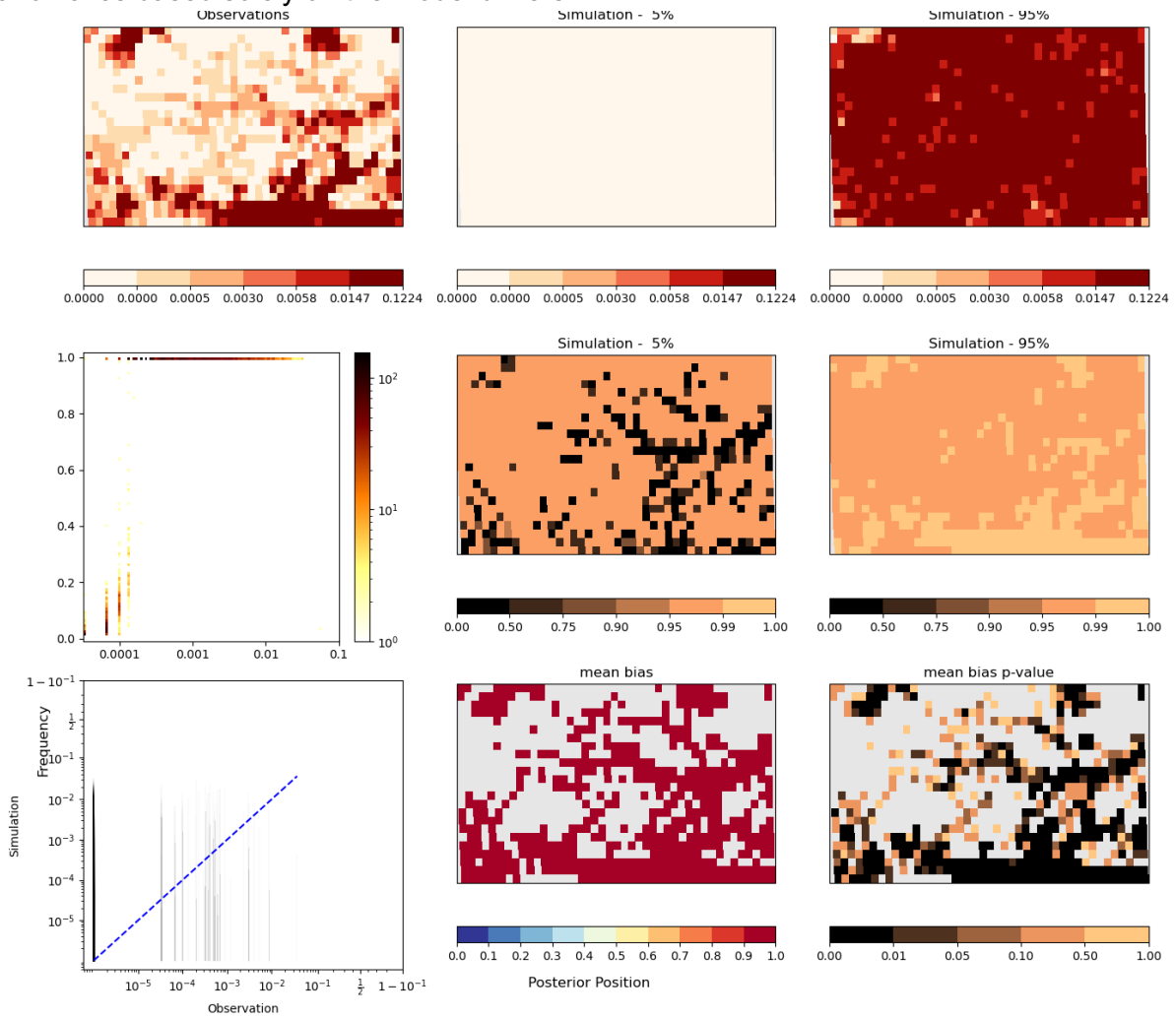
666
 667
 668
 669

Figure S31: same as **Figure S29** but for Greece in August

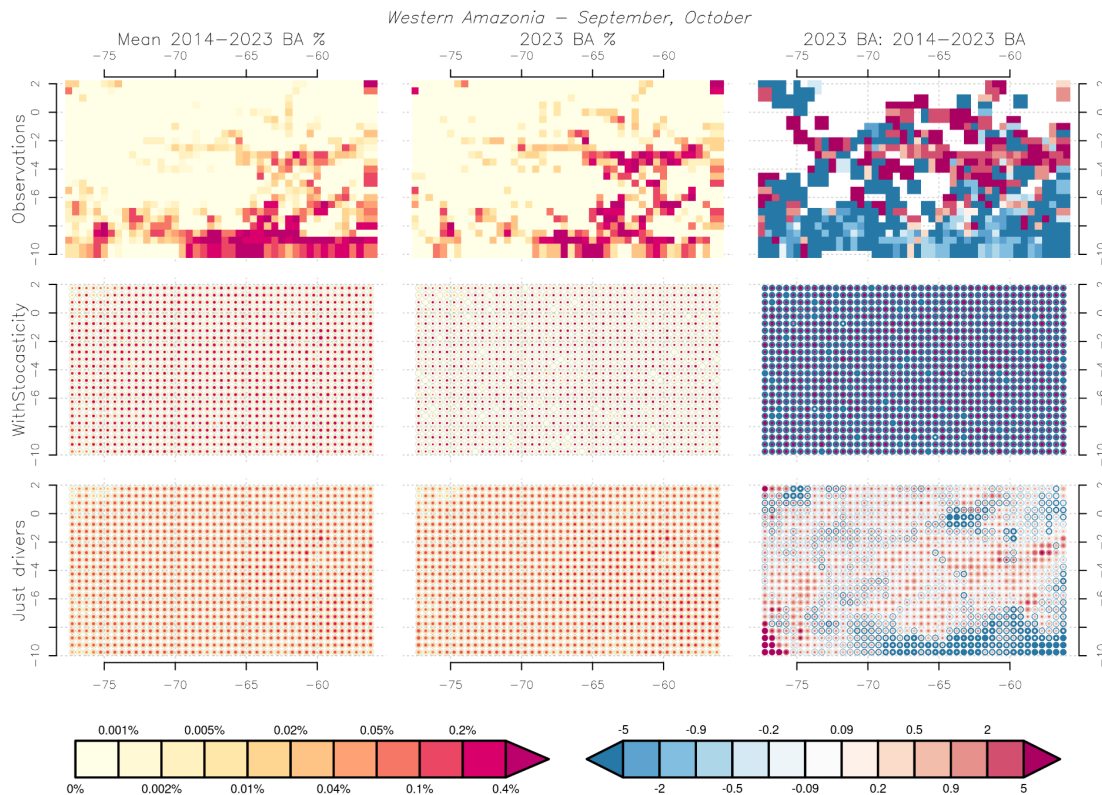
670 Western Amazonia

671 The model captures observations within its uncertainty range, but it fails to differentiate
 672 between high burning in deforestation regions in the south and north of the country. This
 673 suggests that vital data on deforestation and its interaction with fire may have been missed.
 674 The model is able to generate observations out of its sample, indicated by a high likelihood
 675 given observations. However, it does not generate very low BA, particularly in places where

676 high BA are also commonly observed in regions of deforestation. This suggests that the
 677 model may fail to capture variations in BA in these human-dominated areas. Similar to the
 678 other two regions, the model demonstrated a low bias. However it can accurately capture BA
 679 anomalies based solely on the model drivers.



680
 681 **Figure S32: same as Figure S28 for Western Amazonia**
 682
 683



684 **Figure S33:** same as **Figure S29** but for Western Amazonia in September and October.

685
686
687
688
689 **Change in Likelihood of High Burned Area in 2023 due to Total Climate Forcing and**
690 **Socioeconomic factors**

691
692 The framework utilising ISIMIP3a reanalysis data has been found to outperform its near-real-
693 time counterpart in simulating BA. It effectively represents high BA and extremes across all
694 regions. Furthermore, the probability of observations given the model is generally higher in
695 areas with extreme fires or high BA, indicating the model's reliability for attribution analysis.
696

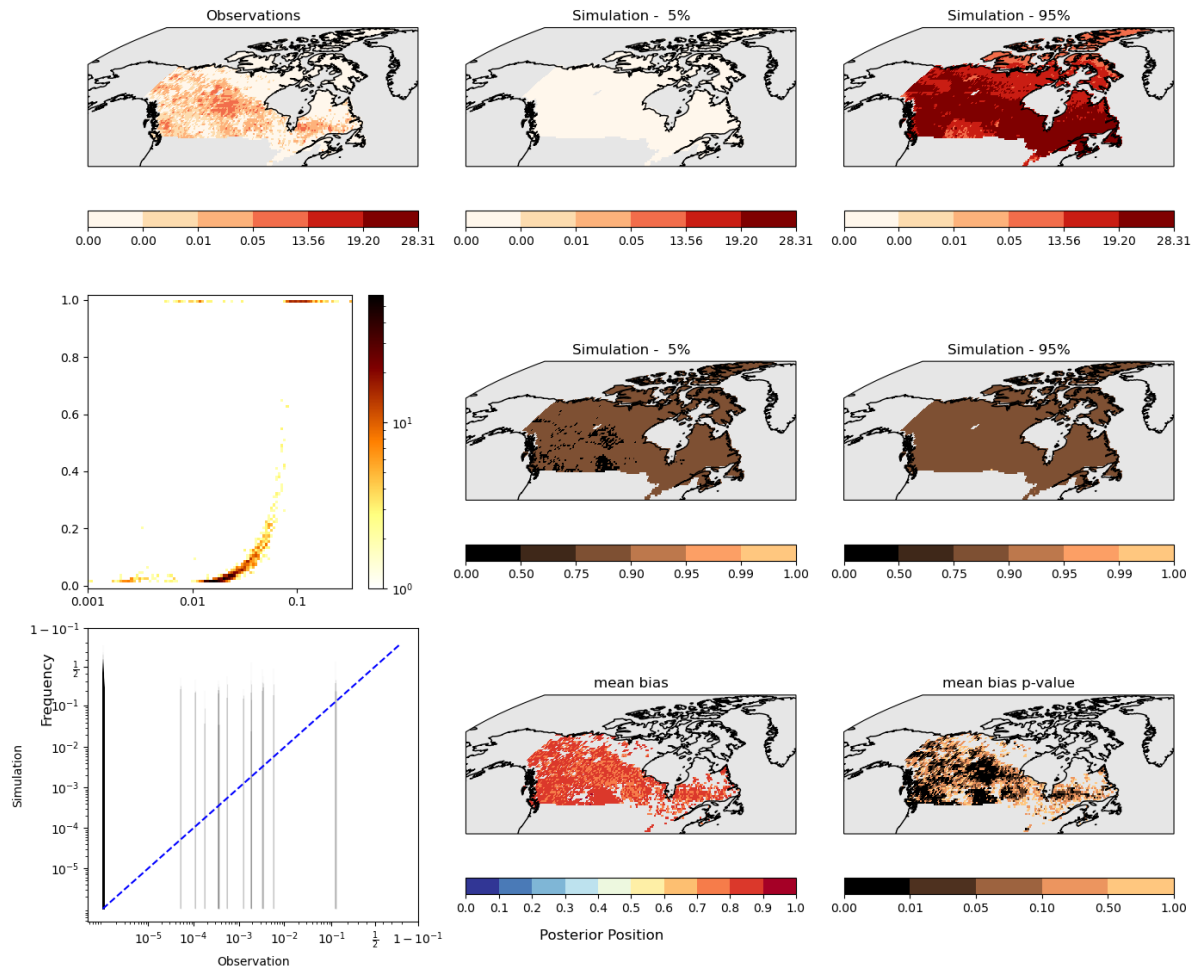
697 However, in regions of significant land use change, such as Western Amazonia, the model
698 struggles with reproducing higher BA, indicating a common challenge across regions in
699 capturing detailed land use interactions.

700
701 While observations consistently fall within range of the model distribution, the model
702 demonstrates consistent low bias. This simple scaling is suggested to align the model with
703 observations, highlighting a need for calibration to improve accuracy across regions.
704
705

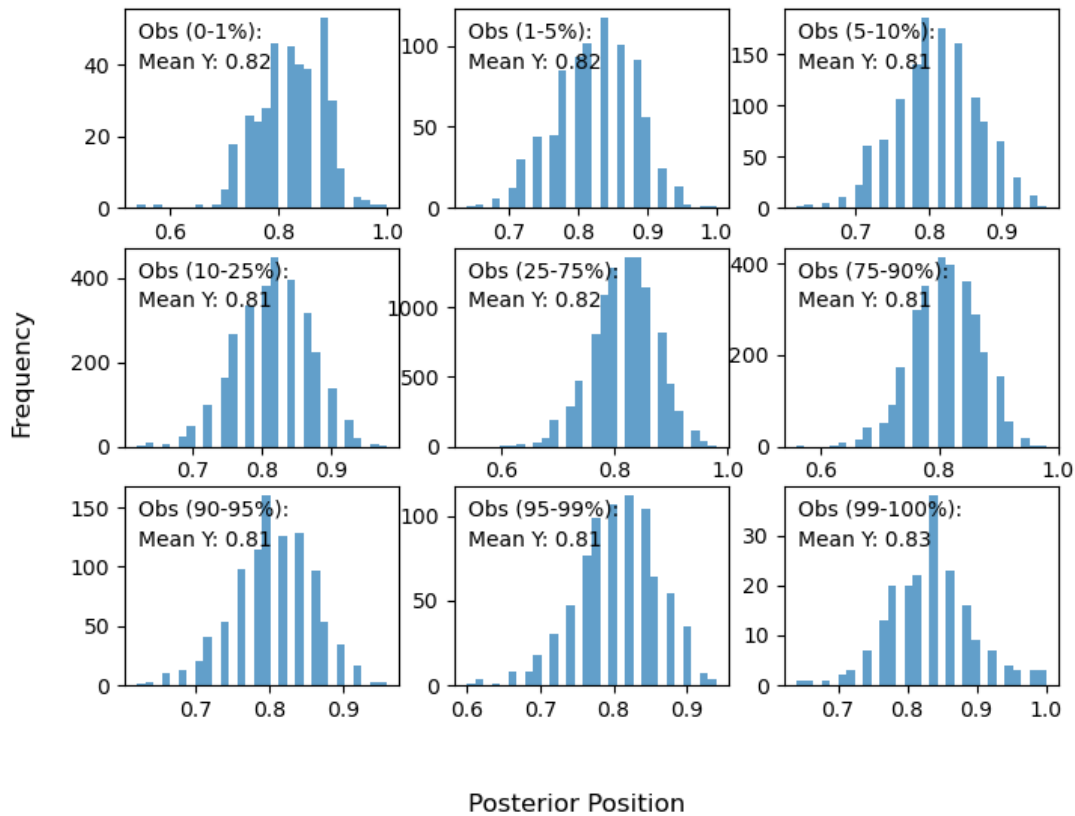
706 **Canada**

707 The analysis using isimip reanalysis data shows that the framework performs much better
708 than its near-real-time counterpart in assessing the drivers of BA (**Figure S34**). Although

709 there are still large uncertainty ranges, the highest BA in the distribution closely match the
 710 high BA observed. In Canada, the model generally performs slightly worse in generating
 711 observations, but it still tends towards a probability of observations given the model of
 712 greater than 0.75. However, the model shows that high BA are very likely, indicating that the
 713 model is useful in representing extremes - critical for attribution analysis. Overall, the model
 714 exhibits less bias than its near real-time version, with observations falling on average around
 715 0.6-0.9 throughout the model's distribution. This consistent pattern across the observed
 716 distribution suggests that a simple scaling is required for attribution application (**Figure 35**).
 717



718 **Figure S34:** same as **Figure S28** for attribution and future projections configuration used in
 719 **section 3.4** and **section 3.5**.
 720

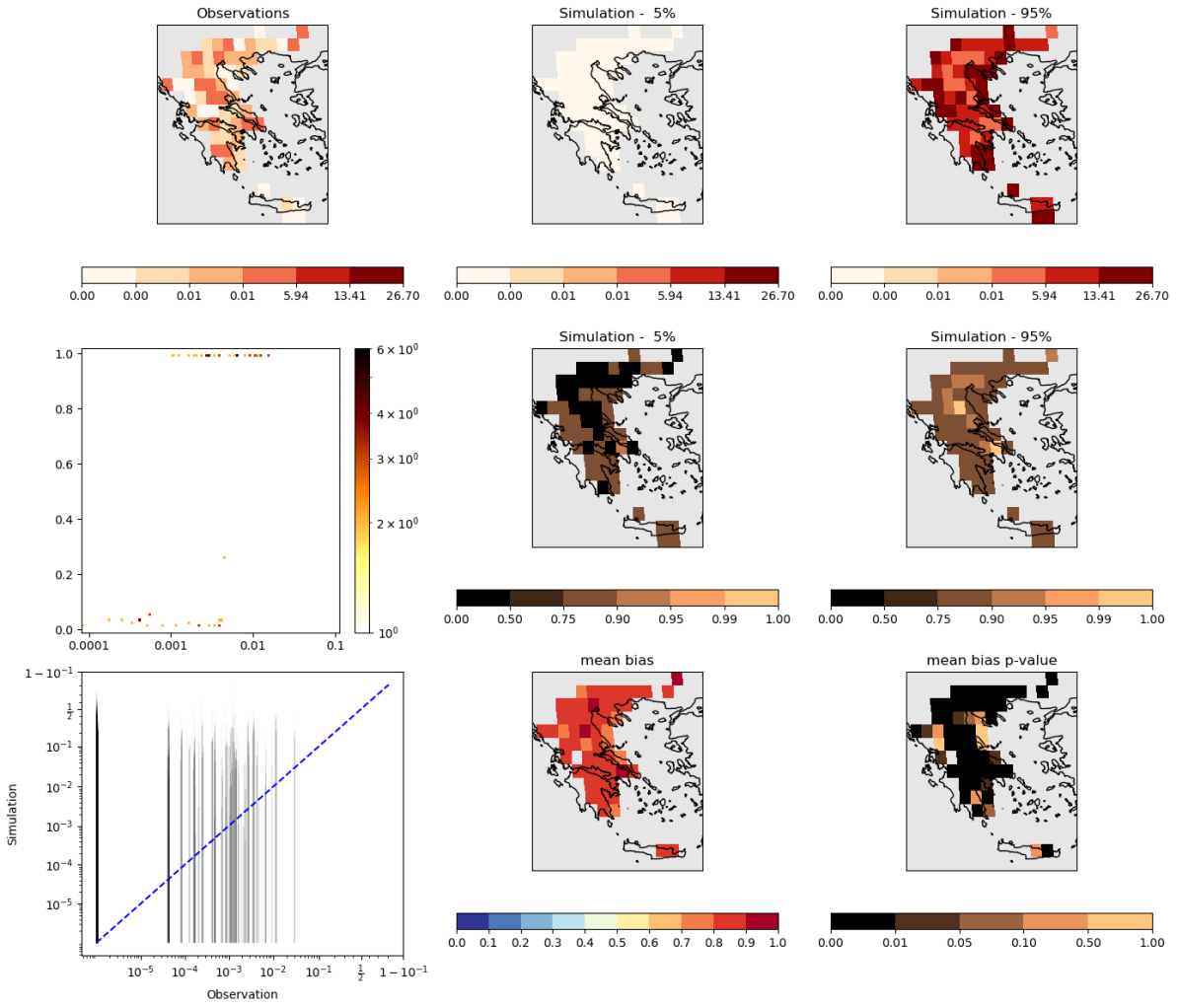


721
722
723
724
725
726

Figure S35: The position of the observed BA in the model's probability distribution over the evaluation period using attribution and future projections configuration from **Section 3.4** and **Section 3.5** over Canada. Histograms are for observed percentiles indicated in the top left corner. See start of section for interpretation guide.

727 **Greece**

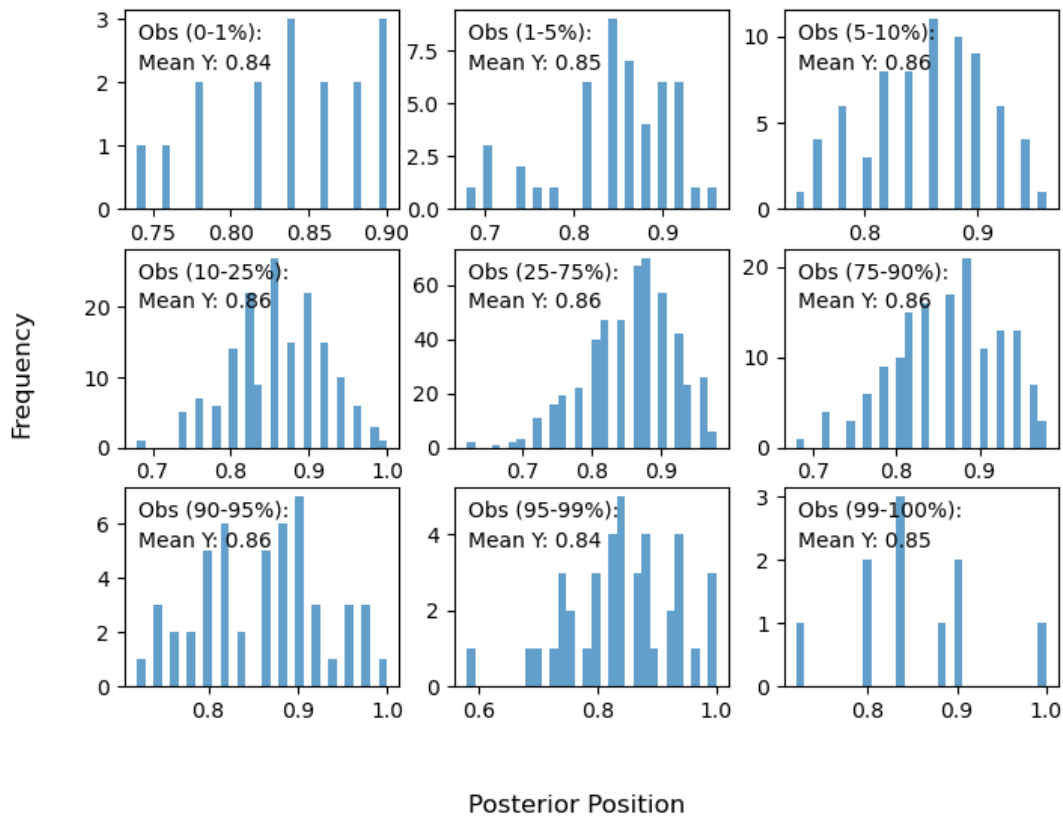
728 Over the longer evaluation periods, observations tend to be much noisier across Greece
729 than in the near real-time driver analysis (**Figure S36**). However, there is still a noticeable
730 trend towards more burning in the Southeast. This trend is well captured by the model,
731 including the more noisy spatial distribution in the observations. The probability of observing
732 a given model can be quite low, but it tends to be higher in areas where extreme fires were
733 observed and in areas with high burn areas, making it useful for attribution applications.
734 Additionally, while the model is biased low, similar to Canada, this bias is consistent across
735 the observed BA distribution (**Figure S37**).
736



737

738

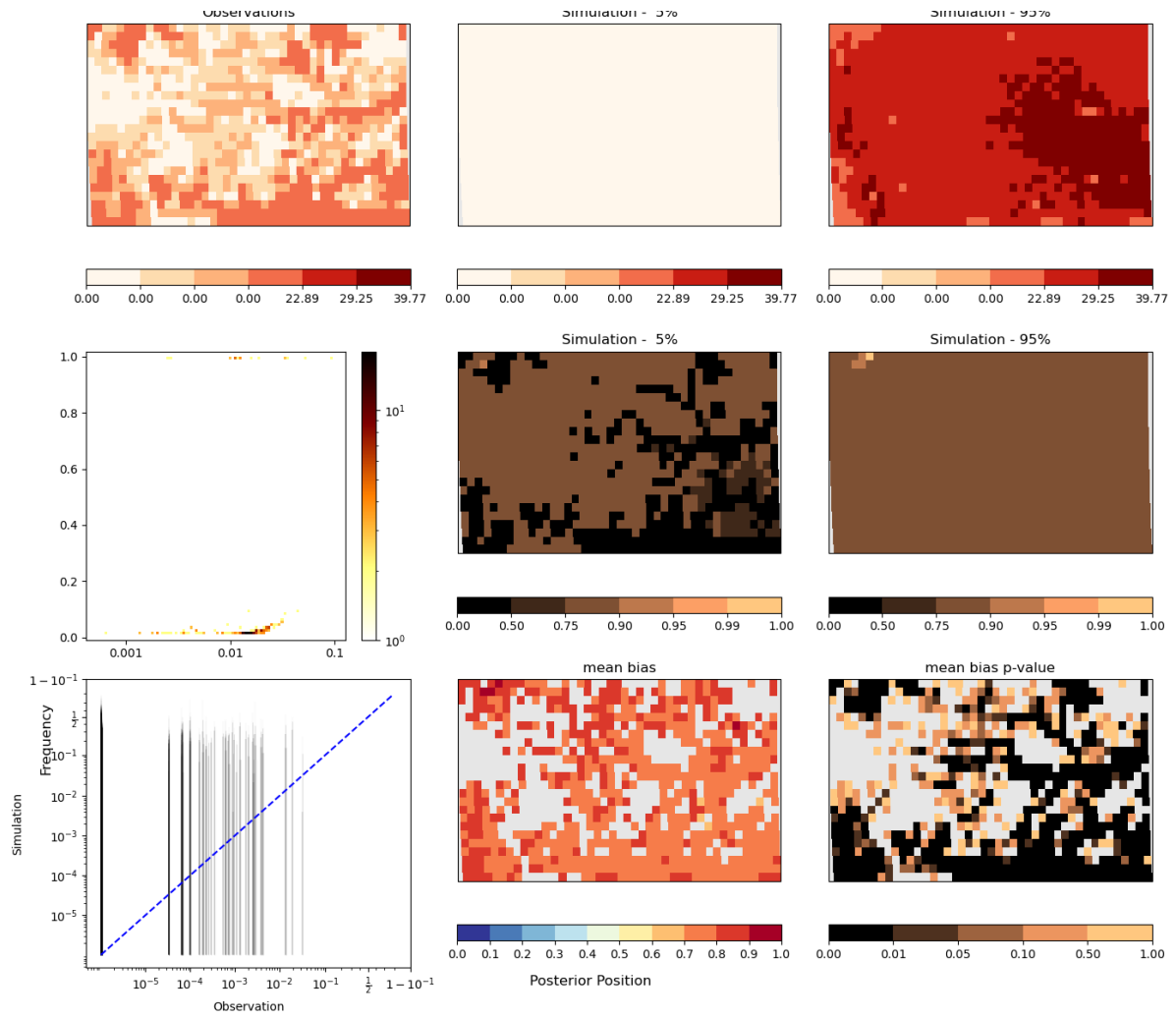
Figure S36: same as **Figure S34** for Greece



739
 740 **Figure S37:** same as **Figure 35** for Greece
 741

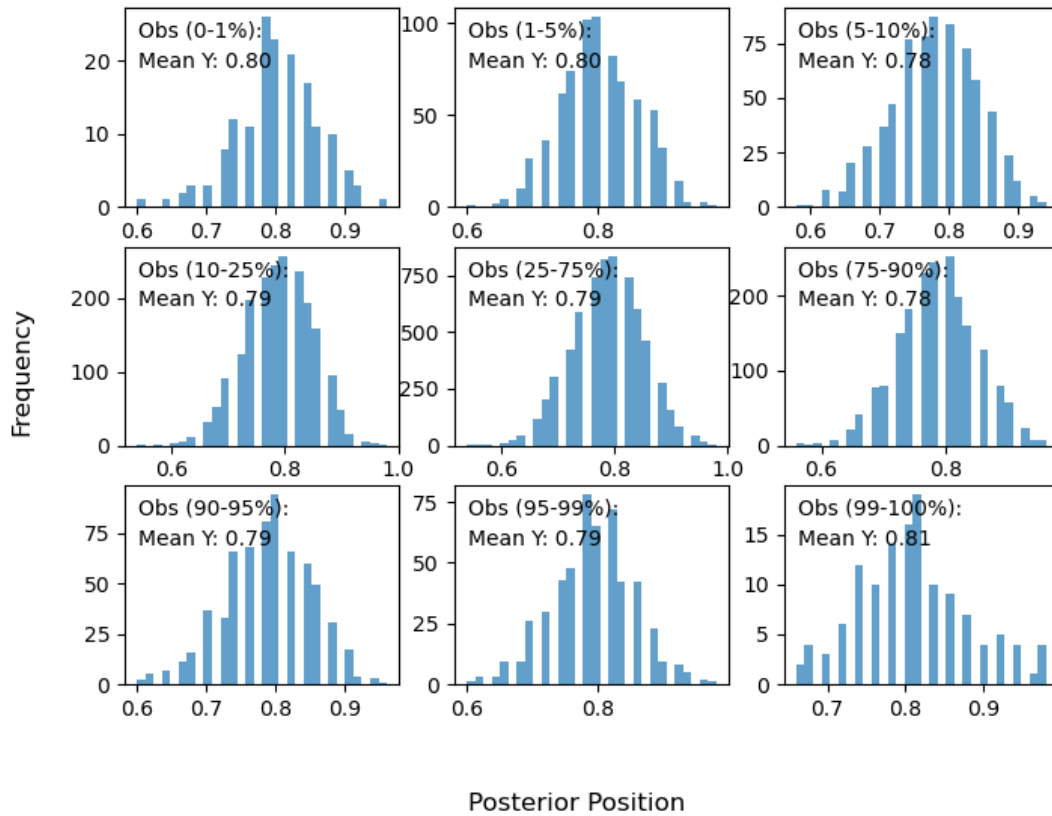
742 **Western Amazonia**

743 The framework outperforms its near real time counterpart in simulating higher BA around
 744 Manaus, although it still struggles to reproduce higher BA in regions of land use change
 745 (**Figure S38**). Observations fall within the model range and, like the other two regions, the
 746 observations indicate that the model tends to perform better at generating observed BA at
 747 higher levels of burning. Overall, this is the least biased region out of the three, although the
 748 model still tends to underestimate BA, with the observations falling at around 0.7-0.8 of the
 749 model distribution (**Figure S39**). This pattern is consistent across the distributions .



750
751

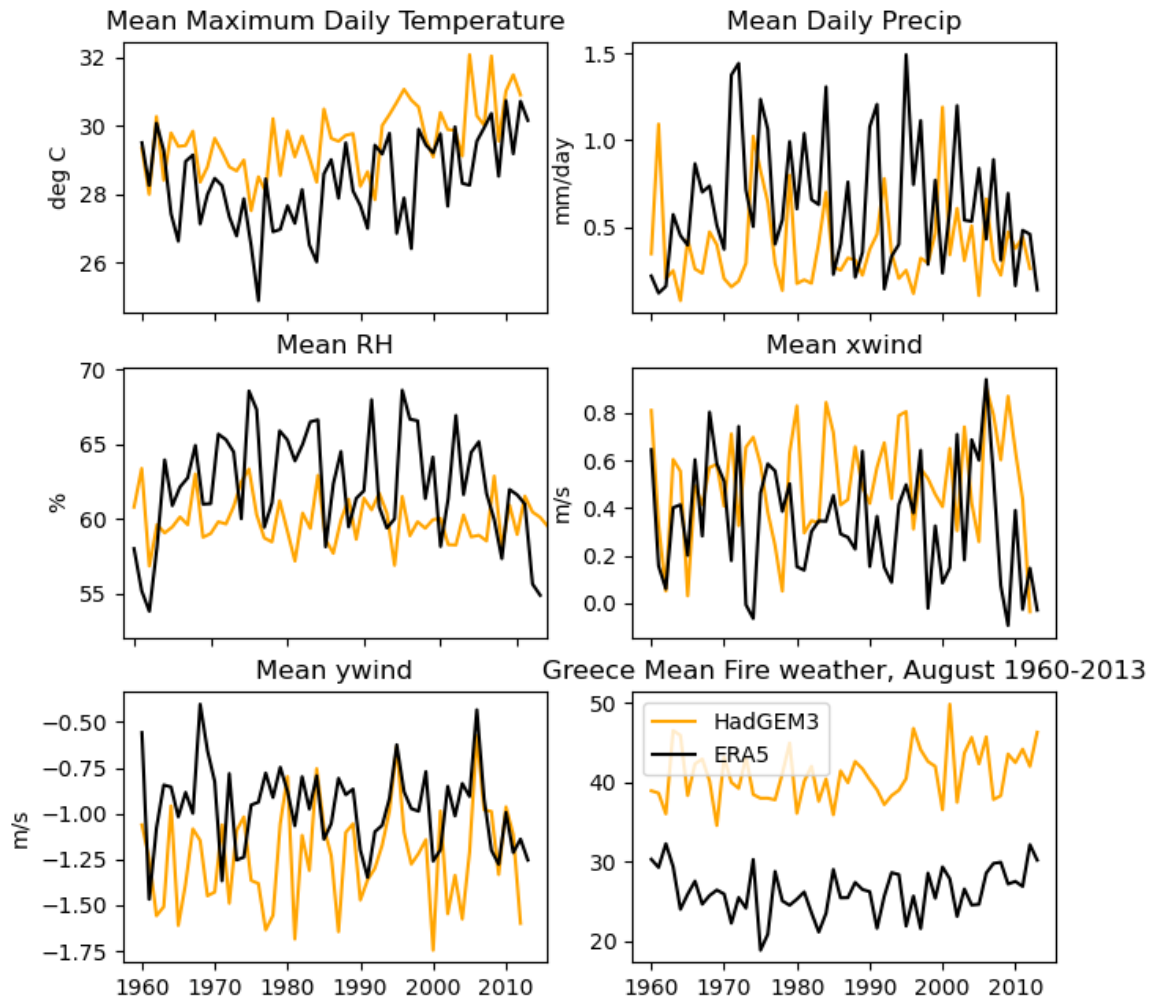
Figure S38: same as **Figure S34** for Western Amazonia.



752
753 **Figure S39:** same as **Figure 35** for Western Amazonia

754
755
756 ***Fire Weather attribution***

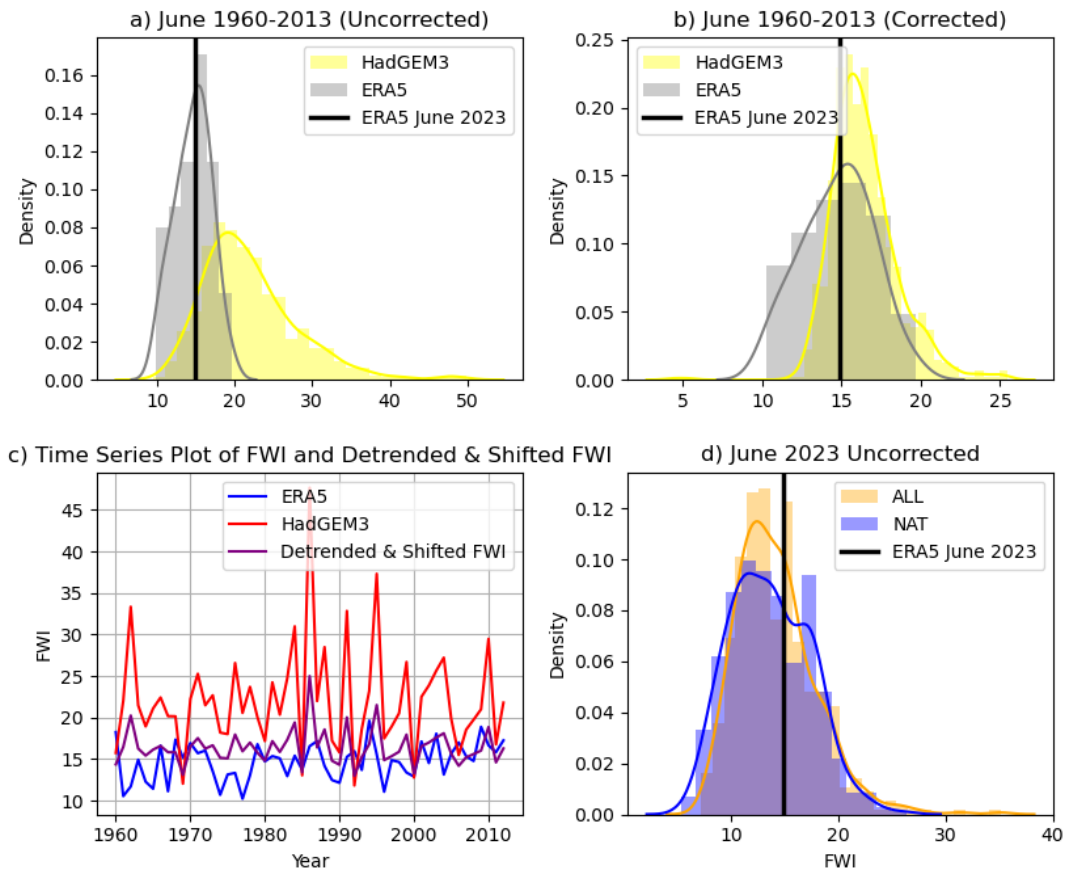
757
758 We evaluated each of the component variables used in the FWI against ERA5 reanalysis for
759 the historical period 1960-2013. In each case, HadGEM3 was slightly biased across the
760 timeseries, generally simulating conditions that were too hot and dry in Greece (**Figure S40**).
761 This led to an overall larger bias in the resultant FWI (**Figure S43**). We therefore applied a
762 linear bias-correction to the HadGEM3 ensemble of FWI (see Data and Data Processing).
763 Results before and after the bias-correction is applied are shown below for each region.



764
765
766
767
768
769
770
771

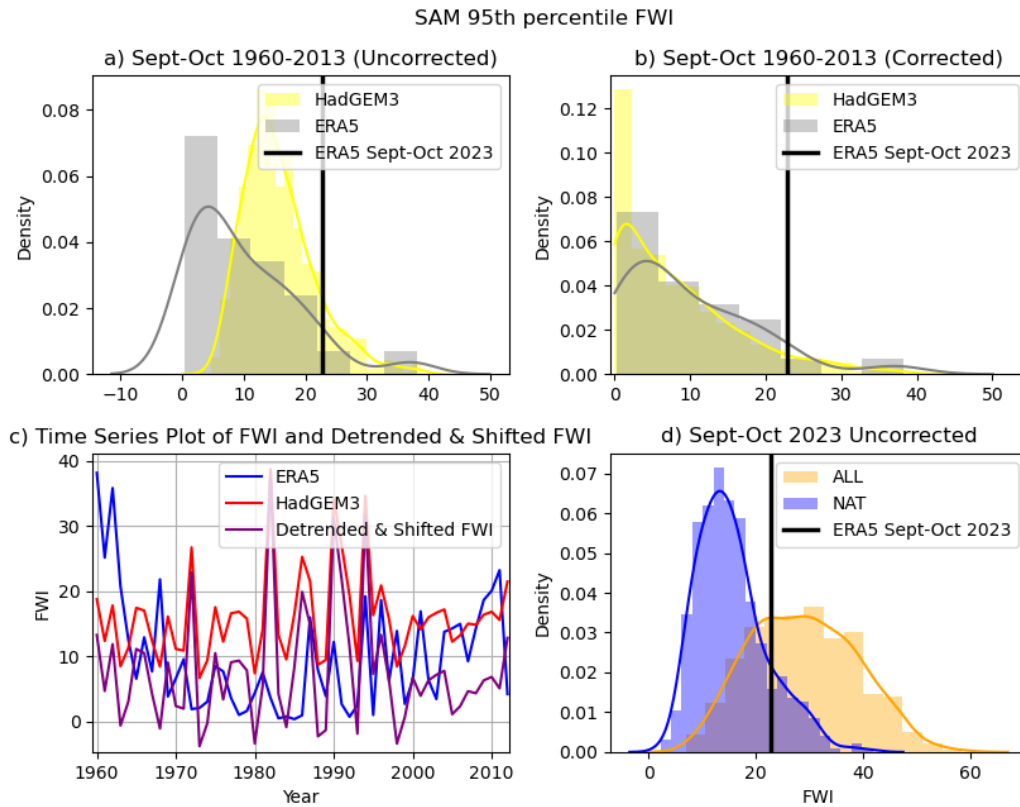
Figure S40: Individual component variables of the FWI compared to ERA5 reanalysis across the historical period (1960-2013), and resultant FWI. Here one member from the HadGEM3 historical ensemble is shown (yellow) against ERA5 (black) for one region (Greece), for illustration

Canada 95th percentile FWI



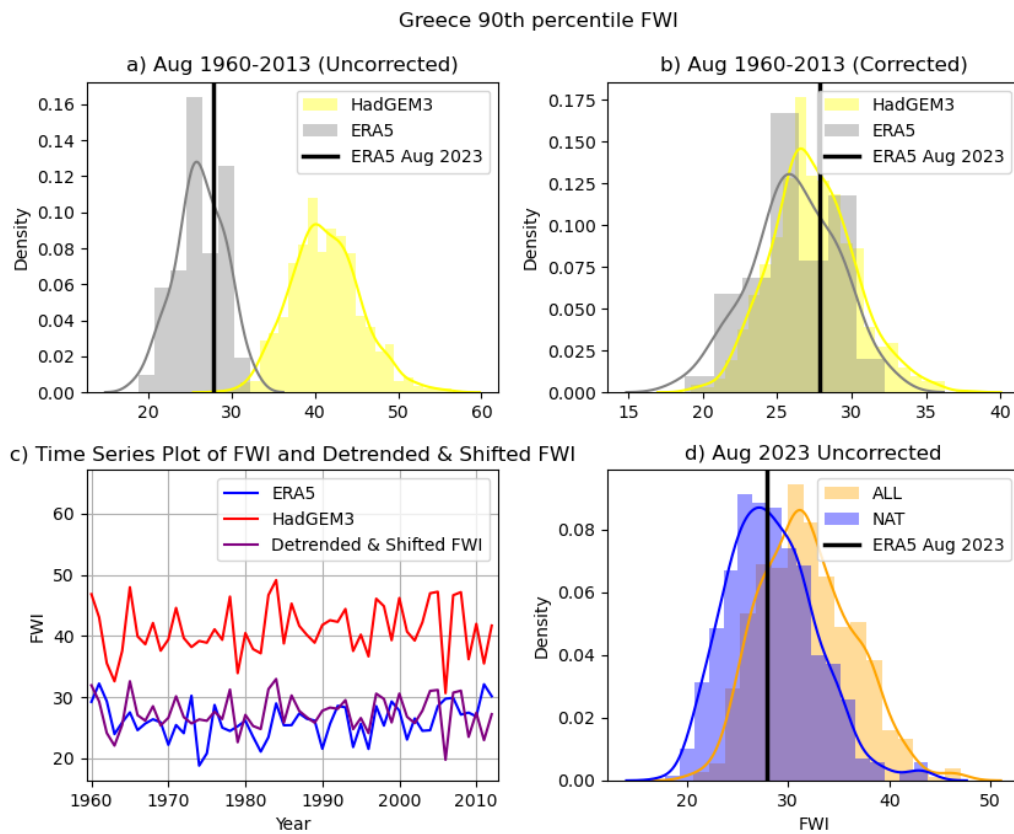
772
773
774
775
776
777
778
779

Figure S41: Bias correction for Canada. Historical ensemble of HadGEM3 (yellow) compared to ERA5 (grey) 95th percentile of FWI for the historical period (1960-2013), shown as probability density before correction (a) and after correction (b), and one member shown as a timeseries (c, where HadGEM3 is shown in red, ERA5 in blue and corrected HadGEM3 in purple). HadGEM3 ensemble for 2023 shown before bias-correction (d). ERA5 2023 event shown as black vertical line on all probability density plots.



780
781
782

Figure S42: As for Figure S41, but for Western Amazonia



783
784
785
786

Figure S43: As for Figure S41, but for Greece at 90th percentile FWI

787

788 **References**

- 789 Abril-Pla, O., Andreani, V., Carroll, C., Dong, L., Fomesbeck, C. J., Kochurov, M., Kumar,
790 R., Lao, J., Luhmann, C. C., Martin, O. A., Osthege, M., Vieira, R., Wiecki, T., and Zinkov,
791 R.: PyMC: a modern, and comprehensive probabilistic programming framework in Python,
792 PeerJ Comput Sci, 9, e1516, 2023.
- 793 Barbosa, M. L. F.: TRACING THE ASHES: UNCOVERING BURNED AREA PATTERNS
794 AND DRIVERS OVER THE BRAZILIAN BIOMES, PhD, Instituto Nacional de Pesquisas
795 Espaciais, 2024.
- 796 Burton, C., Betts, R., Cardoso, M., Feldpausch, T. R., Harper, A., Jones, C. D., Kelley, D. I.,
797 Robertson, E., and Wiltshire, A.: Representation of fire, land-use change and vegetation
798 dynamics in the Joint UK Land Environment Simulator vn4. 9 (JULES), Geoscientific Model
799 Development, 12, 179–193, 2019.
- 800 Burton, C., Betts, R. A., Jones, C. D., Feldpausch, T. R., Cardoso, M., and Anderson, L. O.:
801 El Niño Driven Changes in Global Fire 2015/16, Front Earth Sci. Chin., 8,
802 <https://doi.org/10.3389/feart.2020.00199>, 2020.
- 803 Burton, C., Kelley, D. I., Jones, C. D., and Betts, R. A.: South American fires and their
804 impacts on ecosystems increase with continued emissions, Climate Resilience, 2022.
- 805 Burton, C., Lampe, S., Kelley, D. I., Thiery, W., Hantson, S., Christidis, N., Gudmundsson,
806 L., Forrest, M., Burke, E., Chang, J., and Others: Global burned area increasingly explained
807 by climate change, Preprint at [https://doi.org/10.21203/rs, 3](https://doi.org/10.21203/rs.3.rs2823231/v1), 2023.
- 808 Ciavarella, A., Christidis, N., Andrews, M., Groenendijk, M., Rostron, J., Elkington, M.,
809 Burke, C., Lott, F. C., and Stott, P. A.: Upgrade of the HadGEM3-A based attribution system
810 to high resolution and a new validation framework for probabilistic event attribution, Weather
811 and Climate Extremes, 20, 9–32, 2018.
- 812 Clark, D. B., Mercado, L. M., Sitch, S., Jones, C. D., Gedney, N., Best, M. J., Pryor, M.,
813 Rooney, G. G., Essery, R. L. H., Blyth, E., Boucher, O., Harding, R. J., Huntingford, C., and
814 Cox, P. M.: The Joint UK Land Environment Simulator (JULES), model description – Part 2:
815 Carbon fluxes and vegetation dynamics, Geoscientific Model Development, 4, 701–722,
816 2011.
- 817 Dimiceli, C. and Others: MOD44B MODIS/Terra Vegetation Continuous Fields Yearly L3
818 Global 250m SIN Grid V006 (NASA EOSDIS Land Processes DAAC, 2015), 2015.
- 819 DiMiceli, C. M., Carroll, M. L., Sohlberg, R. A., Huang, C., Hansen, M. C., and Townshend,
820 J. R. G.: Annual global automated MODIS vegetation continuous fields (MOD44B) at 250 m
821 spatial resolution for data years beginning day 65, 2000? 2010, collection 5 percent tree
822 cover, University of Maryland, College Park, MD, USA, 2017.
- 823 European Commission EU Science Hub: Wildfires in the Mediterranean: EFFIS data reveal
824 extent this summer, available at: [https://joint-research-centre.ec.europa.eu/jrc-news-and-](https://joint-research-centre.ec.europa.eu/jrc-news-and-updates/wildfires-mediterranean-effis-data-reveal-extent-summer-2023-09-08_en)
825 [updates/wildfires-mediterranean-effis-data-reveal-extent-summer-2023-09-08_en](https://joint-research-centre.ec.europa.eu/jrc-news-and-updates/wildfires-mediterranean-effis-data-reveal-extent-summer-2023-09-08_en), last
826 access:, 2023.
- 827 Hantson, S., Arneth, A., Harrison, S. P., and Kelley, D. I.: The status and challenge of global
828 fire modelling, 2016.

- 829 Hoffman, M. D. and Gelman, A.: The No-U-Turn Sampler: Adaptively Setting Path Lengths in
830 Hamiltonian Monte Carlo, arXiv [stat.CO], arXiv, 1593–1623,
831 <https://doi.org/10.5555/2627435.2638586>, 2011.
- 832 Huang, H., Xue, Y., Li, F., and Liu, Y.: Modeling long-term fire impact on ecosystem
833 characteristics and surface energy using a process-based vegetation–fire model
834 SSiB4/TRIFFID-Fire v1.0, *Geosci. Model Dev.*, [https://doi.org/10.5194/gmd-2020-122-](https://doi.org/10.5194/gmd-2020-122-supplement)
835 [supplement](https://doi.org/10.5194/gmd-2020-122-supplement), 2020.
- 836 Huang, H., Xue, Y., Liu, Y., Li, F., and Okin, G.: Modeling the short-term fire effects on
837 vegetation dynamics and surface energy in Southern Africa using the improved
838 SSiB4/TRIFFID-Fire model, <https://doi.org/10.5194/gmd-2021-116>, 2021.
- 839 Hugelius, G., Tarnocai, C., Broll, G., Canadell, J. G., Kuhry, P., and Swanson, D. K.: The
840 Northern Circumpolar Soil Carbon Database: spatially distributed datasets of soil coverage
841 and soil carbon storage in the northern permafrost regions, *Earth Syst. Sci. Data*, 5, 3–13,
842 2013.
- 843 Ito, A.: Disequilibrium of terrestrial ecosystem CO₂ budget caused by disturbance-induced
844 emissions and non-CO₂ carbon export flows: a global model assessment, *Earth Syst. Dyn.*,
845 10, 685–709, 2019.
- 846 Kelley, D. I., Bistinas, I., Whitley, R., and Burton, C.: How contemporary bioclimatic and
847 human controls change global fire regimes, *Nat. Clim. Chang.*, 2019.
- 848 Kelley, D. I., Burton, C., Huntingford, C., and Brown, M. A. J.: Low meteorological influence
849 found in 2019 Amazonia fires, 2021.
- 850 Knorr, W., Kaminski, T., Arneth, A., and Weber, U.: Impact of human population density on
851 fire frequency at the global scale, *Biogeosciences*, 11, 1085–1102, 2014.
- 852 Lange, S.: Trend-preserving bias adjustment and statistical downscaling with ISIMIP3BASD
853 (v1.0), *Geosci. Model Dev.*, <https://doi.org/10.5194/GMD-12-3055-2019>, 2019.
- 854 Lehsten, V., Tansey, K., Balzter, H., Thonicke, K., Spessa, A., Weber, U., Smith, B., and
855 Arneth, A.: Estimating carbon emissions from African wildfires, *Biogeosciences*, 6, 349–360,
856 2009.
- 857 Li, F., Zeng, X. D., and Levis, S.: A process-based fire parameterization of intermediate
858 complexity in a Dynamic Global Vegetation Model, *Biogeosciences*, 9, 2761–2780, 2012.
- 859 Li, F., Levis, S., and Ward, D. S.: Quantifying the role of fire in the Earth system – Part 1:
860 Improved global fire modeling in the Community Earth System Model (CESM1),
861 *Biogeosciences*, 10, 2293–2314, 2013.
- 862 Mangeon, S., Voulgarakis, A., Gilham, R., Harper, A., Sitch, S., and Folberth, G.: INFERNO:
863 a fire and emissions scheme for the UK Met Office’s Unified Model, *Geosci. Model Dev.*, 9,
864 2685–2700, 2016.
- 865 Mathison, C., Burke, E., Hartley, A. J., Kelley, D. I., Burton, C., Robertson, E., Gedney, N.,
866 Williams, K., Wiltshire, A., Ellis, R. J., Sellar, A. A., and Jones, C. D.: Description and
867 evaluation of the JULES-ES set-up for ISIMIP2b, *Geoscientific Model Development*, 16,
868 4249–4264, 2023.
- 869 McNorton, J. and Di Giuseppe, F.: A global fuel characteristic model and dataset for wildfire
870 prediction, *Biogeosciences*, <https://doi.org/10.5194/bg-21-279-2024>, 2024.

- 871 Melton, J., Arora, V., Wisernig-Cojoc, E., Seiler, C., Fortier, M., Chan, E., and Teckentrup,
872 L.: CLASSIC v1.0: the open-source community successor to the Canadian Land Surface
873 Scheme (CLASS) and the Canadian Terrestrial Ecosystem Model (CTEM) – Part 1: Model
874 framework and site-level performance, *Geosci. Model Dev.*, 13, 2825–2850, 2020.
- 875 Mengel, M., Treu, S., Lange, S., and Frieler, K.: ATTRICI v1. 1--counterfactual climate for
876 impact attribution, *Geoscientific Model Development*, 14, 5269–5284, 2021.
- 877 Moritz, M. A., Morais, M. E., Summerell, L. A., Carlson, J. M., and Doyle, J.: Wildfires,
878 complexity, and highly optimized tolerance, *Proc. Natl. Acad. Sci. U. S. A.*, 102, 17912–
879 17917, 2005.
- 880 Rabin, S. S., Melton, J. R., and Lasslop, G.: The Fire Modeling Intercomparison Project
881 (FireMIP), phase 1: experimental and analytical protocols with detailed model descriptions,
882 *Geoscientific Model*, 2017.
- 883 Schroeder, W., Oliva, P., Giglio, L., and Csiszar, I. A.: The New VIIRS 375 m active fire
884 detection data product: Algorithm description and initial assessment, *Remote Sensing of*
885 *Environment*, 143, 85–96, <https://doi.org/10.1016/j.rse.2013.12.008>, 2014.
- 886 Sellar, A. A., Jones, C. G., and Mulcahy, J. P.: UKESM1: Description and evaluation of the
887 UK Earth System Model, in *Modeling Earth ...*, 2019.
- 888 Smith, B., Wårlind, D., Arneth, A., Hickler, T., Leadley, P., Siltberg, J., and Zaehle, S.:
889 Implications of incorporating N cycling and N limitations on primary production in an
890 individual-based dynamic vegetation model, *Biogeosciences*, 11, 2027–2054, 2014.
- 891 Spuler, F., Wessel, J., Comyn-Platt, E., Varndell, J., and Cagnazzo, C.: ibicus: a new open-
892 source Python package and comprehensive interface for statistical bias adjustment and
893 evaluation in climate modelling (v1.0.1), *Geosci. Model Dev.*, [https://doi.org/10.5194/gmd-](https://doi.org/10.5194/gmd-17-1249-2024)
894 [17-1249-2024](https://doi.org/10.5194/gmd-17-1249-2024), 2024.
- 895 Thonicke, K., Venevsky, S., Sitch, S., and Cramer, W.: The role of fire disturbance for global
896 vegetation dynamics: coupling fire into a Dynamic Global Vegetation Model, *Glob. Ecol.*
897 *Biogeogr.*, 10, 661–677, 2001.
- 898 Thonicke, K., Spessa, A., Prentice, I. C., Harrison, S. P., Dong, L., and Carmona-Moreno,
899 C.: The influence of vegetation, fire spread and fire behaviour on biomass burning and trace
900 gas emissions: results from a process-based model, *Biogeosciences*, 7, 1991–2011, 2010.
- 901 UNEP, Popescu, A., Paulson, A. K., Christianson, A. C., Sullivan, A., Tulloch, A., Bilbao, B.,
902 Mathison, C., Robinson, C., Burton, C., Ganz, D., Nangoma, D., Saah, D., Armenteras, D.,
903 Driscoll, D., Hankins, D. L., Kelley, D. I., Langer, E. R. L., Baker, E., Berenguer, E., Reisen,
904 F., Robinne, F.-N., Galudra, G., Humphrey, G., Safford, H., Baird, I. G., Oliveras, I., Littell, J.,
905 Kieft, J., Chew, J., Maclean, K., Wittenberg, L., Anderson, L. O., Gillson, L., Plucinski, M.,
906 Moritz, M., Brown, M., Soto, M. C., Flannigan, M., Costello, O., Silva, P. S., Fernandes, P.,
907 Moore, P., Jandt, R., Bianchi, R., Libonati, R., Archibald, S., Dunlop, S., McCaffrey, S.,
908 Page, S., Gonzãfãlez, T. D. T., Sokchea, T., and Charlton, V.: Spreading like Wildfire: The
909 Rising Threat of Extraordinary Landscape Fires, edited by: Sullivan, A., Kurvits, T., and E.,
910 B., United Nations Environment Programme and GRID-Arendal., 2022.
- 911 Xanthopoulos, G., Zevgoli, E., Kaoukis, K., and Athanasiou, M.: Greece - Lessons not
912 learned, available at: [https://issuu.com/wildfiremagazine-](https://issuu.com/wildfiremagazine-iawf/docs/wildfire_magazine_q4_2023_-_web)
913 [iawf/docs/wildfire_magazine_q4_2023_-_web](https://issuu.com/wildfiremagazine-iawf/docs/wildfire_magazine_q4_2023_-_web), last access:, *Wildfire*, 2023, 2024.
- 914 Yue, C., Ciais, P., Cadule, P., Thonicke, K., Archibald, S., Poulter, B., Hao, W., Hantson, S.,

915 Mouillot, F., Friedlingstein, P., Maignan, F., and Viovy, N.: Modelling the role of fires in the
916 terrestrial carbon balance by incorporating SPITFIRE into the global vegetation model
917 ORCHIDEE – Part 1: simulating historical global burned area and fire regimes, *Geoscientific*
918 *Model Development*, 7, 2747–2767, 2014.

919 Yue, C., Cadule, P., and Van Leeuwen, T. T.: Modelling the role of fires in the terrestrial
920 carbon balance by incorporating SPITFIRE into the global vegetation model ORCHIDEE--
921 Part 2: Carbon emissions and the role of fires in the global carbon balance, *Geoscientific*
922 *Model Development*, 8, 1321–1338, 2015.

923